UNIVERSITY OF COPENHAGEN
FACULTY OF SCIENCE
NIELS BOHR INSTITUTE

Master's Thesis

Non-adiabatic effects in the relaxation of a Vaidya black hole

Jakov Mozetič

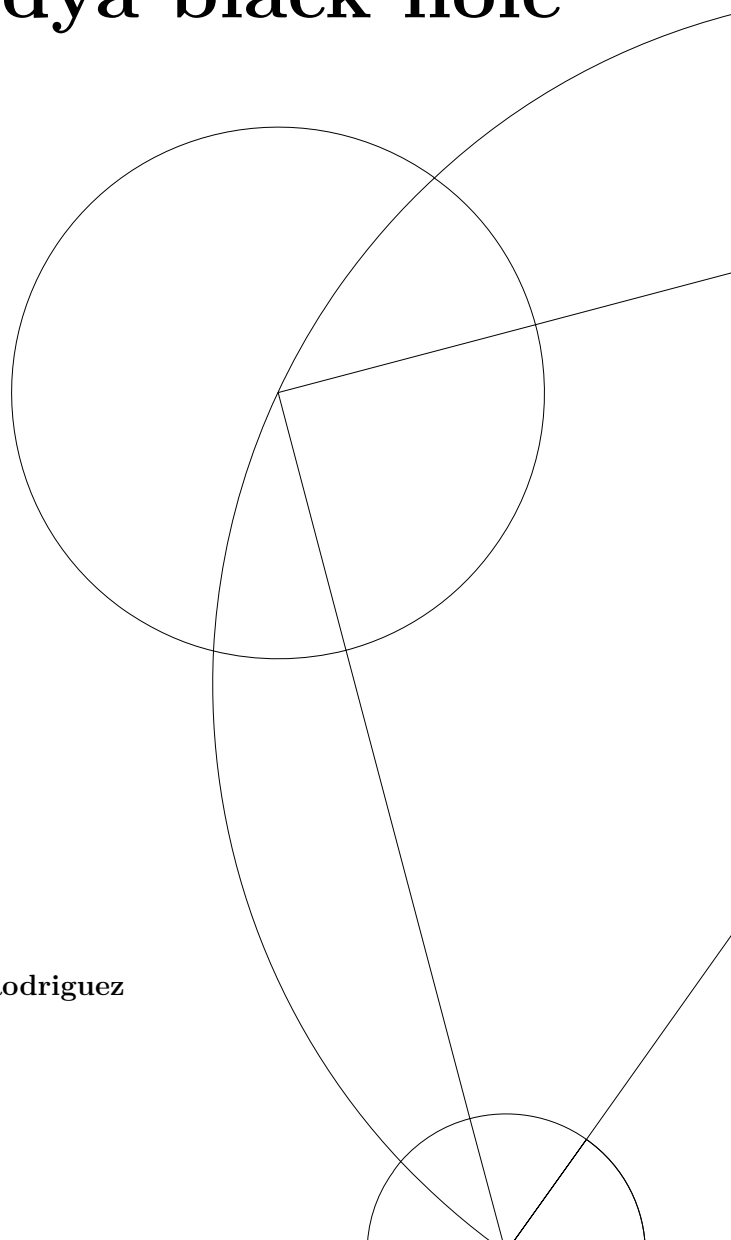

Supervisors: Troels Harmark, David Pereñiguez Rodriguez

May 19, 2025

Acknowledgments

I am very grateful to my supervisors, Troels and David, for proposing such an interesting topic and guiding me through every step of this endeavor. I would also like to thank all the members of the Center of Gravity at the Niels Bohr Institute for very interesting discussions on gravitational-wave phenomena during our weekly meetings.

A special thanks goes to my parents, who have supported me throughout my entire educational journey and always believed in my goals, and to my brother, sister, and grandmother for their constant encouragement. Finally, I thank all my friends at the Niels Bohr Institute—and beyond—for an exceptional two years filled with inspiring conversations about science, beer, the science of beer, and much more. I could not have done it without you.

Abstract

General Relativity's non-linear nature can be probed by studying gravitational waves from black hole spacetimes. Standard waveform models do not include non-linear effects, such as mass and spin change of the black hole, motivating their closer study. In this thesis, we focus on the effects induced by a mass change of a black hole. These effects are present in many physical scenarios: black holes in astrophysical environments, in the post-merger ringdown, after a collapse of a neutron star, and many more. We investigate the black hole gravitational-wave signature in the form of quasinormal modes. We model the mass change using Vaidya spacetime, a relatively simple framework that captures the essential features of the problem even at first order. Specifically, this project focuses on understanding non-adiabatic effects in quasinormal modes induced by these mass changes. We find that non-adiabatic effects follow a single, universal behavior for many different accretion processes. In the high-frequency limit, we find a simple relation, which provides a foundation for incorporating non-adiabatic effects into future gravitational-wave analysis.

Contents

1 Introduction

Black holes (BHs) and gravitational waves (GW) were unforeseen predictions of Einstein's theory of gravity, The General Theory of Relativity (GR). Next to being unique to the theory, BHs are the most basic objects that the theory allows, requiring only the fundamental constants of GR, Newton's gravitational constant G, speed of light c, plus their mass (spin and charge) to be described [1]. In Section 2 we will see how these constants alone set the gravitational radius, which fixes the black holes size. Because of their unique and minimal nature in GR, their thorough theoretical study is highly motivated and makes them perfect objects for testing the theory. In the starting years, many theories were developed surrounding BHs and GWs [1–6], and in the 20th century, experimental techniques were developed to confirm the existence of black holes [7]. With the recent development of gravitational wave detectors, we were able to detect the other unique solution [8], giving us a completely different, but equally powerful way to confirm the theory. Since GR is a non-linear theory of gravity, its solutions tell us how the spacetime behaves in extreme regimes. Black holes are objects that are so gravitationally compact that the spacetime around them is in this strong-filed regime. This is the reason why GW from BHs offer a window into such phenomena, motivating closer study of the possible effects associated with them.

The most observed GW come from a merger of two black holes [8], presented in Figure 1.1 [9]. There are three regimes of GW emission during the merger: inspiral, the very merger

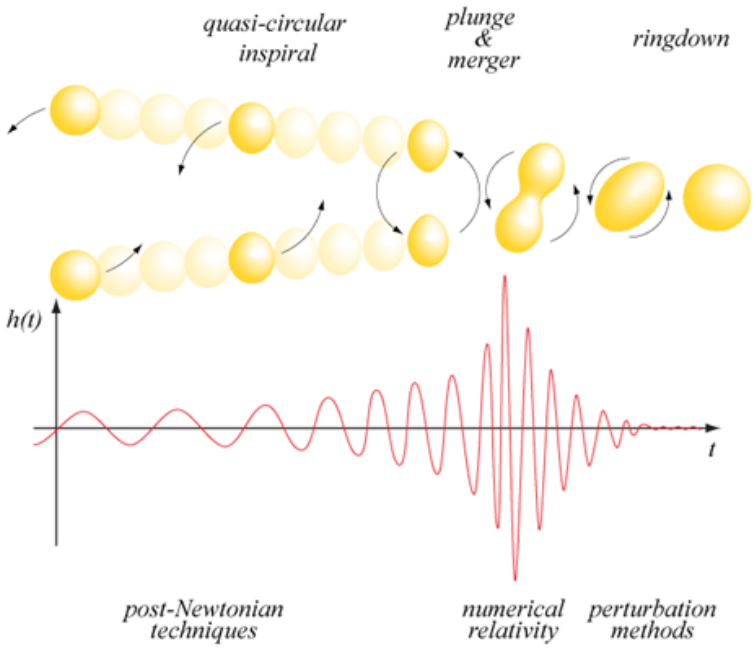

Figure 1.1: Schematic representation of a merger of two black holes [9]. Three regimes are highlighted alongside the techniques used to obtain their solution.

and ringdown [8]. Solutions for the inspiral are obtained by post-Newtonian techniques [10, 11] and are comparably simple to describe analytically. The very point of the merger is highly non-linear and notoriously hard to describe analytically, so numerical relativity techniques [12] are used to obtain solutions describing it. Once the merger is over, the black hole goes into

a ringdown stage, which is is modeled by black hole perturbation theory (BHPT) [5, 6, 13, 14], describing a black hole oscillating and approaching a static state. Since these models describe one phenomena with three different approaches, some analytic some numerical, each one requires its own in depth analysis. Numerical relativity solutions show that the mass and spin of the black hole change right after the merger [15, 16], giving insight into what physical effects should be considered in BHPT. The ringdown is usually modeled by taking the final mass of the black hole to be constant, restricting its description to $t \sim 10 - 15m$ after the merger [17], where m is the black holes mass. Introduction of non-linear effects can probe into the region that static models cannot describe, giving us a more accurate description of the whole merger process. So, next to an interest in probing the fundamental nature of GR by including non-linear effects, the most observed phenomena in GW physics also supports the interest in extending the black hole perturbation theory by allowing these non-linear effects to take place. In this project we will focus on the extension of black hole perturbation theory. The solutions of the equations obtained from BHPT are damped sinusoids, where the loss of energy is due to the event horizon (and spatial infinity), allowing the black hole to reach a static state [3, 5, 11]. These oscillation modes are called quasinormal modes (QNMs) and are oscillating in natural frequencies of the black hole. QNMs are fundamental phenomena in black hole spacetimes since the associated quasinormal frequencies (QNFs) hold information about their main features: mass, charge, and spin [11]. Since these modes decay exponentially, it is challenging to accurately measure them experimentally [18]. Nonetheless, black hole perturbation theory models this ringdown process quite well, and since QNMs are connected to the fundamental properties of black holes, their study is crucial for proper description of effects inscribed in GR. The usual way of studying them has limitations, as they are not capturing non-linear effects such as changes in the QNFs due to mass and spin change. In this thesis, will focus specifically on extending this by studing effects induced by a mass change.

The analysis of gravitational waves as perturbations in a black hole background has been theoretically studied long before we had means of measuring these waves, laying the foundations of the theory [3–6]. In the early stages, black hole perturbation theory has been studied for a static spherically symmetric black hole [5, 6]. By now, it has been thoroughly studied for many types of perturbations, such as scalar, vector and gravitational [11]. We have techniques for obtaining their frequency and decay time with high precision [3], and waveform models describing them [8]. Black hole perturbation theory has also been extensively studied for rotating black holes [3, 19], which is one of few possible extensions of the Schwarzschild black hole. QNMs are also used in AdS/CFT correspondence [20] and as fundamental properties in many extensions of GR [21]. Furthermore, there have been studies that place black holes in astrophysical environment [22], further generalizing the theory to describe a wide range of physical scenarios that can occur in nature. The placement of a black hole in an astrophysical environment poses a similar question that numerical relativity already pointed at: What if the black hole accretes some of the mass (or energy) orbiting it during its relaxation? A well known result from black hole perturbation theory is that its QNFs, often assigned a symbol ω, measured in the scale determined by the BH mass are a set of fixed values $m\omega = const.$ [3, 11]. The scale is set by the BHs mass due to the fact that the mass remains the only dimensional parameter in the system

after going to geometric units ($c = 1, G = 1$). Since this is true for any static black hole, it poses as a natural benchmark while exploring the effects induced by a mass change. But, once the mass changes the whole picture of perturbation theory conceptually breaks down, and the question is whether we can model these effects with time-changing frequencies. If we can, do these time-changing QNFs follow $m(t)\omega(t) = const.$, and if they don't, are there any regular imprints on the QNFs connected to this mass change? This question is exactly what we will try to answer in this project.

The mass change is notoriously hard to model, requiring going to third order perturbation theory. At second order we can capture the effects of absorption of QNMs into the horizon, changing the black hole mass and spin, which is then captured by third order coupling between the modes [23]. In this project, we will use a comparably simple model describing accretion to a black hole, allowing us to describe the essential features of mass accretion already at first order. The spacetime used is Vaidya spacetime [24], which is only restricted by the assumption that the spacetime is close to spherical symmetry. This spacetime was already considered with the goal describing its QNMs [25, 26]. Physical processes that this spacetime can model are more than a few. One of them is the aforementioned black holes in astrophysical environments [22]. Furthermore, numerical relativity has identified this mass change in the scattering of waves in BH spacetimes, head-on collisions of BHs, and in the ringdown stage [15, 16]. Also, mass change is present in the collapse of neutron stars [27]. These are some processes where the mass is accreted, but Vaidya black hole is also used to describe Hawking radiation [28], a famous process of evaporation of a black hole [29].

The thesis is organized as follows: in Section 2 we will show how black holes and gravitational waves arise from the theory and introduce the key concepts and physical phenomena associated with them. In Section 3 we will introduce black hole perturbation theory and obtain covariant equations governing perturbations in spherically symmetric spacetimes with arbitrary matter content. We will then comment on their general properties, boundary conditions and the nature of the solutions. Then, from the equations obtained from BHPT, we will be able to calculate QNFs for a static black hole, which will serve as reference points in the study of a mass-changing black hole. After having an understanding of QNMs, the corresponding QNFs and their description in the static case, we will turn to the analysis of a mass-chaning black hole, presented in Section 4. We will first introduce the spacetime modeling a mass-changing black hole and comment on its origins and physical meaning. Having an intuition of this spacetime, we will consider its representation in double-null coordinates and extract its perturbation equations of the gravitational sector. Having the equations governing the dynamics we are interested in, we will turn to solving them. Since equations coming from black hole perturbation theory are known to be quite involved and hard to solve analytically, we will present a numerical technique used for obtaining solutions. With these solutions in hand, we will analyze the inertial behavior in the extracted QNFs, confirming some results in the literature [25, 26] and uncovering new features in the non-adiabatic regime. Our analysis will show a well behaved inertial behavior, allowing us to generalize it to many different dynamical spacetimes. The main result will be the description of non-adiabatic process in the eikonal limit, but we will also explore how this process reacts to changes of other properties of the background. This will lead us to a unified

description of the non-adiabatic behavior of QNMs induced by a mass change of a black hole.

2 Gravitational waves and black holes

In this section we will see how gravitational waves and black holes materialize in Einstein's General Theory of Relativity. Dynamics in the theory are governed by the Einstein field equations:

$$G_{\mu\nu} \equiv R_{\mu\nu} - \frac{1}{2} g_{\mu\nu} R = \frac{8\pi G}{c^4} T_{\mu\nu} - \Lambda g_{\mu\nu}, \tag{2.0.1}$$

which tell us how the spacetime is influenced by matter and energy content and vice versa. On the left we have objects that hold information about the curvature of spacetime, where $G_{\mu\nu}$ is the Einstein tensor, $R_{\mu\nu}$ is the Ricci tensor and R is the Ricci scalar. On the right is the energy-momentum tensor $T_{\mu\nu}$ and the cosmological constant Λ, which hold information about the matter and energy content of the spacetime. Information about how matter and energy determine the geometry of spacetime (and vice versa) is encoded in the metric $g_{\mu\nu}$.

To start with, we will focus on a flat space background to introduce key features of gravitational waves [30]. Then, we will introduce solutions to the Einstein field equations (2.0.1) for spherically-symmetric objects, which will lead us to the black hole solution and allow us to inspect its properties [1]. After that, we will consider black hole perturbation theory, the theory describing gravitational waves propagating in black hole backgrounds [14]. Lastly, we will consider solutions to the perturbation equations for a static spherically symmetric black hole and calculate its QNFs. Results from this section will give us relevant equations governing the dynamics we are interested in, and we will have values of QNFs for a static black hole, which will be used as a reference for the rest of this project.

2.1 Gravitational waves in flat space

Gravitational waves arise from the Theory of General Relativity when considering an additional contribution to the background metric, while imposing the weak field limit on this contribution [30]. In this section we will focus on the Minkowski background, so the weak field approximation takes the form:

$$g_{\mu\nu}(x) = \eta_{\mu\nu} + h_{\mu\nu}(x), \tag{2.1.1}$$

where $\eta_{\mu\nu}(x) = (-,+,+,+)$ is the Minkowski metric and $h_{\mu\nu}(x)$ is our weak field, where the weak field condition is imposed with:

$$|h_{\mu\nu}(x)| \ll 1. \tag{2.1.2}$$

Next step is to expand the Einstein filed equations to first order in $h_{\mu\nu}(x)$, which provides us with equations for linearized gravity, with the linearized Ricci tensor:

$$R_{\mu\nu} = \frac{1}{2}\left(\partial^\lambda \partial_\mu h_{\nu\lambda} + \partial^\lambda \partial_\nu h_{\mu\lambda} - \Box h_{\mu\nu} - \partial_\mu \partial_\nu h^\lambda{}_\lambda\right). \tag{2.1.3}$$

Additionally, there is a gauge freedom in our choose of coordinates, and it can be shown that the Ricci tensor is invariant under such transformations [30]. Imposing the Lorentz gauge in

which $h_{\mu\nu}$ obeys:

$$\partial^{\mu}\left(h_{\mu\nu}-\frac{1}{2}\eta_{\mu\nu}h^{\rho}_{\rho}\right)=0, \tag{2.1.4}$$

we arrive to linearized Einstein filed equations in Lorentz gauge:

$$\Box h_{\mu\nu}=-16\pi\left(T_{\mu\nu}-\frac{1}{2}\eta_{\mu\nu}\eta^{\rho\sigma}T_{\rho\sigma}\right). \tag{2.1.5}$$

Setting $T_{\mu\nu}=0$ we arrive to a free wave equation:

$$\Box h_{\mu\nu}=0, \tag{2.1.6}$$

which describes an relativistic wave equation for each component $h_{\mu\nu}$. We can consider the ansatz:

$$h_{\mu\nu}(x)=A_{\mu\nu}e^{ik_{\rho}x^{\rho}}, \tag{2.1.7}$$

subject to the following conditions:

$$k_{\mu}k^{\mu}=0, \quad A_{\mu\nu}=A_{\nu\mu}, \quad k^{\mu}A_{\mu\nu}=0, \quad A_{\mu 0}=0, \quad \eta^{\mu\nu}A_{\mu\nu}=0, \tag{2.1.8}$$

where first one comes from the equations of motion, the second one from the fact that the theory is symmetric in μ and ν, and the last three from gauge conditions. These conditions reduce the degrees of freedom from the maximal 10 (16 if we hide the fact that the theory is a priori symmetric in μ and ν), down to 2. These degrees of freedom correspond to well known polarizations of gravitational waves h_{+} and $h_{\times}$. Final result has the following form:

$$h_{\mu\nu}=\mathrm{Re}\left[A_{\mu\nu}e^{ik_{\rho}x^{\rho}}\right], \tag{2.1.9}$$

and this wave solution for the metric is called a gravitational wave.

To source gravitational waves, we need to have a distribution of matter whose dynamics lead to dissipation of energy. This is described by the quadrupole formula [30]:

$$\langle P\rangle_t=\frac{1}{5}\langle\dddot{Q}_{ij}\dddot{Q}_{ij}\rangle_{t-r}, \quad r\gg\tau\gg d^{1}, \tag{2.1.10}$$

where $\langle P\rangle_t$ in average total energy flux across a sphere of constant t. $Q_{ij}=I_{ij}-\frac{1}{2}I_{kk}\delta_{ij}$ where I_{ij} is the second moment of energy density. This equation is valid in the radiation zone, enforced by the conditions in (2.1.10). For spherically symmetric spacetimes $Q_{ij}=0$, so there is no quadrupole moment, and no emission of GW. Interestingly, we can source gravitational waves in a spherically symmetric spacetime whenever there is an effective potential barrier outside the object's surface (and some external perturbation to excite it), as is the case for black holes [11]. This process of emission is going to be the main focus of this project.

[1] These conditions enforce the detection in the radiation zone.
d- time it takes light to cross the region containing the matter
r-place of detection
τ-timescale on which $T^{\mu\nu}$ is varying

2.2 Black holes

Before continuing with gravitational waves, we need to introduce the main object of study in this project, a black hole. To achieve this, we consider a spherically symmetric solution for Einstein filed equation, leading us to the solutions describing a black hole and its properties.

2.2.1 Static spherically symmetric spacetime

A static spherically symmetric spacetime has a general line element [1]:

$$ds^2 = -e^{\alpha(r)}dt^2 + e^{\beta(r)}dr^2 + r^2 d\Omega^2, \tag{2.2.1}$$

where $d\Omega^2 = d\theta^2 + \sin^2\theta d\phi^2$. Plugging this line element into Einstein filed equation's and imposing that there is no matter or energy surrounding the object by setting $T^{\mu\nu} = 0$ we obtain:

$$ds^2 = -\left(1 - \frac{r_0}{r}\right)dt^2 + \frac{dr^2}{1 - \frac{r_0}{r}} + r^2 d\Omega^2. \tag{2.2.2}$$

This metric is known as the Schwarzchild metric, where r_0 is an integration constant. We can see that this constant has to have units of length, and using the Newtonian limit we can fix $r_0 = 2GM/c^2$ where M is the total mass as measured for $r \gg r_0$ [1]. This position in our spacetime is known as the Schwarzchild radius, gravitational radius or the position of event horizon. The solution (2.2.2) is unique for these types of spacetimes, enforced by the Birkhoffs theorem, which states that any spherically symmetric solution of the vacuum field equations should be isometric to a patch of Schwarzschild's solution. Line element (2.2.2) will describe a black hole if the whole mass of the object is inside r_0, making it comparable in size to its gravitational radius. These objects are the simplest non-trivial solutions in GR, since they are effectively pure spacetime. This simplicity is enforced by the fact that to describe them, we only need constants representing fundamental scales of the theory, in addition to BHs mass M. These constants of nature are Newton's gravitational constant G and the speed of light c, which we set to $G = c = 1$ for the remainder of the project. We can add spin (ruining the spherical-symmetry) and charge to extend this idea, where the no-hair theorem of black holes prevents us from having more complicated black holes [1]. For stars and other objects that are also described by (2.2.2), r_0 is smaller than the size of the object, making them more complicated than just pure spacetime and requiring a matter model to describe the interior. Because of BHs fundamental place in the theory, they have been the center of study for the whole lifespan of GR. In the first years of GR, black holes were nothing more than a theoretical curiosity, where their experimental discovery also showed their importance in confirming the theory.

We will now explore some of the properties of static spherically-symmetric black holes, emphasizing the ones that will change when we introduce a mass-changing black hole. First, this spacetime has two Killing vectors, $T^\mu = (1, 0, 0, 0)$ and $J^\mu = (0, 0, 0, 1)$, which generate an isometry of the spacetime metric and correspond to a conserved quantity. This is apparent when considering that the coordinates t and ϕ are not explicitly present in our line element. We can notice that at r_0, the timelike Killing vector has zero norm, giving an alternative definition of the horizon [31].

Additionally, there are two special properties of this spacetime that become apparent when considering null trajectories. These null trajectories are defined by $ds^2 = 0$ and obeyed by massless matter (such as light and gravitational waves). When we inspect the equations of the outgoing null curves inside the horizon, we observe that they cannot escape the black hole. This fact with play a key role when setting the boundary conditions for QNMs. Furthermore, null matter always travels at the speed of light in vacuum, allowing the creation of a unique place outside the horizon, called the light-ring [11]. This is a place where tangential null trajectories to the angular coordinate always remain on a fixed distance from the black hole. In other words, they orbit the black hole indefinitely. This radius is exactly at $r = 3M$ for a Schwarzschild solution.

One more property that becomes apparent when approaching the event horizon $r = 2M$ is that the spatial part of the metric blows up to infinity. This is know as a coordinate singularity, as it can be transformed away by introducing a new set of coordinates. Usually, this is done by introducing Eddington-Finkelstein (EF) coordinates, and we start the transformation to them by first introducing the tortoise coordinate:

$$r_*(r) = r + r_0 \ln\left|\frac{r}{r_0} - 1\right|, \tag{2.2.3}$$

where:

$$\frac{dr}{dr_*} = 1 - \frac{r_0}{r}. \tag{2.2.4}$$

This coordinate is widely used in GR because it maps the event horizon singularity from $r = 2M$ to $r_* \to -\infty$. To get to the metric in EF coordinates, we have to introduce two new coordinates based on r_* and t:

$$u = t - r_*, \quad v = t + r_*, \tag{2.2.5}$$

where $v = const.$ corresponds to infalling radial null curves, and $u = const.$ to outgoing radial null curves. Now, the line element in advanced EF coordinates reads:

$$ds^2 = -\left(1 - \frac{r_0}{r}\right)dv^2 + 2dvdr + r^2 d\Omega^2. \tag{2.2.6}$$

We can observe that this metric does not posses the infinity of the radial component of the metric when approaching r_0, as we had in (2.2.2), showing it is not a genuine singularity.

2.2.2 Vaidya black hole

Once we have described a static spherically-symmetric solution to Einstein filed equations, we can loosen the static requirement to allow a mass change of a black hole. To achieve this, we can simply promote the constant mass in coordinates (2.2.6) to a function of v (remembering $r_0 = 2M$), leading us to the following line element:

$$ds^2 = -\left(1 - \frac{2M(v)}{r}\right)dv^2 + 2dvdr + r^2 d\Omega^2. \tag{2.2.7}$$

Crucially, this metric still obeys Einstein filed equations, with the energy-momentum tensor:

$$T_{\mu\nu} = 2\frac{\partial_v M(v)}{r^2} K_\mu K_\nu, \quad K_\mu dx^\mu = -dv, \tag{2.2.8}$$

where K^2 are null fields. The metric (2.2.7) with the energy-momentum tensor (2.2.8) describe a so called *pure radiation field*, or *null dust* solution to Einstein filed equations [32]. We will go in detail about this spacetime in Section 4.1.1. For now, we can comment on how the properties of this black hole differ from the static case. First, these is no longer a time-like Killing vector, since we have an explicit dependence on the "time" coordinate v in our metric. Second, the light-ring is no longer well defined. While the mass change is happening, there are no longer null trajectories tangential to the angular coordinate that remains tangential forever. As we will see, we will still be able to obtain the properties of the source by considering the "instantaneous" position of the ling-ring. Lastly, by introducing the change of mass, we are no longer in vacuum, since the additional energy contributing to this mass change is in the vicinity of the black hole. This violates Birkhoffs theorem and makes this spacetime a bit more interesting to investigate. With the definition of the spacetimes we are interested in, we can turn to obtaining equations describing their perturbations.

3 Black hole perturbation theory

The goal of this section is to connect black holes and gravitational waves and see what phenomena occurs when they meet in the same physical scenario. We will start by introducing the equations governing gravitational waves in a black hole background, and then describe what physical conditions we need to introduce to solve these equations. This will lead us to quasinormal modes as natural solutions to these equations. In the end, we will go through a calculation of QNFs for a static black hole, giving us reference points for the mass-changing black hole.

3.1 Gravitational waves in a spherically-symmetric spacetime

In this section, we will promote the flat space considered in section (2.1) to a spherically-symmetric spacetime with the goal of obtaining the equations governing dynamics of gravitational waves propagating in a black hole spacetime. This analysis is commonly called black hole perturbation theory [11]. We will introduce a procedure for obtaining the linearized Einstein filed equations for the gravitational sector in a covariant and gauge invariant formalism [14]. This formalism will lead us to a covariant wave equation plus a covariant equation for energy-momentum tensor. We will use the results of this section to consider GW of two spacetimes in multiple coordinate systems. This analysis closely follows [13, 14].

All the spacetimes considered in this project are of the form:

$$ds^2 = \hat{g}_{\mu\nu} dx^\mu dx^\nu = g_{ab}(y) dy^a dy^b + r^2(y) \Omega_{AB}(z) dz^A dz^B. \tag{3.1.1}$$

This is a line element of a most general spherically symmetric background. The line element lives on a spacetime manifold $\mathcal{M}$ that is a warped product of a two-dimensional Lorentzian

manifold $\mathcal{N}^2$ and the unit 2-sphere $\mathbb{S}^2$. The 2-dimansional manifold $\mathcal{N}^2$ is parametrized by a coordinate y^a where a runs from 0 to 1, where $g_{ab}(y)$ is a Lorenzian metric. The manifold of a unit 2-sphere $\mathbb{S}^2$ is parametrized by z^A where A runs from 2 to 3. Ω_{AB} is a metric of a unit 2-sphere and $r^2(y)$ is a function defined on $\mathcal{N}^2$. We will raise and lower indices with g_{ab} and Ω_{AB}. Covariant derivatives will be denoted by $\hat{\nabla}$, ∇ and D for $\hat{g}_{\mu\nu}$, g_{ab} and Ω_{AB}, respectively. In this spacetime, the most general energy momentum tensor takes the form:

$$T = T_{ab}(y)dy^a dy^b + r^2(y)\mathcal{T}(y)\Omega_{AB}(z)dz^A dz^B, \tag{3.1.2}$$

where $T_{ab}(y)$ and $\mathcal{T}(y)$ are a symmetric tensor and a function on $\mathcal{N}^2$, respectively. This line element and energy-momentum tensor can now be substituted into Einstein filed equations, which leads us to:

$$G_{ab} + \frac{H}{r^2}g_{ab} - \frac{2}{r}(\nabla_a r_b - \nabla_c r^c g_{ab}) = T_{ab}, \tag{3.1.3}$$

$$\frac{\nabla_a r^a}{r} - \frac{R}{2} = \mathcal{T}, \tag{3.1.4}$$

where $r_a r^a = 1 + H(y)$ and $\Lambda = 0$. Additionally, the conservation of energy-momentum tensor for this spacetime satisfies:

$$\nabla^b(r^2 T_{ba}) - 2r\mathcal{T}r_a = 0. \tag{3.1.5}$$

With the general properties and equations for this spacetime, we turn to the method for obtaining equations governing its linear perturbations. We approach this problem by applying Hodge's theorem on the 2-sphere. The theorem states that on a manifold with the structure introduced above, one can do a harmonic decomposition of tensor fields. This leads us to the following decomposition of the metric fluctuations h and energy-momentum fluctuations θ:

$$h = h^L_{ab}Y^L dy^a dy^b + 2[h^L_a Z^L_A + j^L_a X^L_A]dy^a dz^A + [j^L W^L_{AB} + k^L U^L_{AB} + m^L V^L_{AB}]dz^A dz^B, \tag{3.1.6}$$

$$\theta = \theta^L_{ab}Y^L dy^a dy^b + 2[\theta^L_a Z^L_A + \rho^L_a X^L_A]dy^a dz^A + [\rho^L W^L_{AB} + \theta^L U^L_{AB} + \sigma^L V^L_{AB}]dz^A dz^B, \tag{3.1.7}$$

where Y^L is the usual spherical harmonic on the round 2-sphere, Z^L_A, U^L_{AB} and V^L_{AB} are even tensor harmonics, and X^L_A and W^L_{AB} are odd sector tensor harmonics, discussed in Appendix A. Additionally, we need to introduce the gauge parameter:

$$\xi = \xi^L_a Y^L dy^a + [\xi^L Z^L_A + \chi^L X^L_A]dz^A. \tag{3.1.8}$$

The gauge transformations generated by ξ are:

$$h_{\mu\nu} \to h_{\mu\nu} - 2\hat{\nabla}_{(\mu}\xi_{\nu)}, \delta T_{\mu\nu} \to T_{\mu\nu} - \mathcal{L}_\xi T_{\mu\nu}. \tag{3.1.9}$$

To take these into account, we can construct an h-dependent vector field $\eta[h]$ which transform under a gauge transformation as $\eta_\mu \to \eta_\mu + \xi_\mu$ [13, 14]. From this, one can construct gauge

invariant variables associated to metric and energy-momentum fluctuations:

$$\tilde{h} = (h_{\mu\nu} + 2\hat{\nabla}_{(\mu}\eta_{\nu)})dx^{\mu}dx^{\nu}, \tag{3.1.10}$$

$$\tilde{\theta} = (\theta_{\mu\nu} + \mathcal{L}_{\eta}T_{\mu\nu})dx^{\mu}dx^{\nu}. \tag{3.1.11}$$

$$\tag{3.1.12}$$

With the gauge invariant variables describing metric and energy-momentum transformations, we can go to the linearized Einstein filed equations:

$$E_{\mu\nu} \equiv \delta\hat{G}_{\mu\nu} - \delta T_{\mu\nu} = S_{\mu\nu}, \tag{3.1.13}$$

where $S_{\mu\nu}$ is some external first order source. Since $E_{\mu\nu}$ are gauge invariant, we can set $\eta_{\mu} = 0$ and then promote the result to the gauge-invariant variables. The equations resulting from this are quite involved and I point the reader to [14] for detailed expressions for all the components of linearized Einstein filed equations. On a spherically symmetric background the linearized Einstein filed equations $E_{\mu\nu}$ split into two sectors [5, 13, 14], where the decoupling is associated with invariance under parity, as seen from the decomposition in spherical harmonics (Appendix A). Also, the two sectors are isospectral at first order [11, 13]. This justifies studding them separately, and in this work we only consider the axial (odd) sector. Set of equations governing it are (omitting the even parts represented by $\dots$):

$$E_{aA} = \Big\{r^{-2}\,\nabla^{b}\big(r^{4}\nabla_{[a}v_{b]}\big) + \frac{\lambda^{2}-2}{2}\,v_{a} + r^{2}P\,v_{a} - \tilde{\rho}_{a}\Big\}X_{A} + \dots \equiv O_{a}\,X_{A} + \dots, \tag{3.1.14}$$

$$E_{AB} = \big(\nabla_{a}(r^{2}v^{a}) - \tilde{\rho}\big)\,W_{AB} + \cdots \equiv OW_{AB} + \dots, \tag{3.1.15}$$

where $\lambda^{2} = \ell(\ell+1)$. We now we define source terms Υ^{L}_{a} and Υ^{L} as angular integrals of the energy-momentum tensor:

$$O^{L}_{a} = \Upsilon^{L}_{a} = \frac{1}{\lambda^{2}}\int d\Omega\bar{X}^{LA}S_{aA}, \tag{3.1.16}$$

$$O^{L} = \Upsilon^{L} = 2\frac{(l-2)!}{(l+2)!}\int d\Omega\bar{W}^{LAB}S_{AB}. \tag{3.1.17}$$

Since we will focus on the odd sector, will only need the presented odd parts of the equations plus the vector part of the energy-momentum tensor conservation. Using completeness relations of tensor harmonics and the normalizations of Y^{L} chosen to be $\int_{S^{2}} d\Omega\bar{Y}^{L'}Y^{L} = \delta_{L'L}$ we arrive to the following three coupled equations:

$$r^{-2}\nabla^{b}(r^{4}\nabla_{[a}v_{b]}) + \frac{(\lambda^{2}-2)}{2}v_{a} + r^{2}\mathcal{T}v_{a} - \tilde{\rho}_{a} = \Upsilon_{a}, \tag{3.1.18}$$

$$\nabla_{a}(r^{2}v^{a}) - \tilde{\rho} = \Upsilon, \tag{3.1.19}$$

$$\nabla_{a}[r^{2}(\rho^{a} - \tilde{r^{2}}\mathcal{T}v^{a})] + \frac{(2-\lambda^{2})}{2}\tilde{\rho} = -\nabla_{a}(r^{2}\Upsilon^{a}) - \frac{(2-\lambda^{2})}{2}\Upsilon. \tag{3.1.20}$$

We can observe that we have reduced the equations governing the dynamics to a set of PDEs on $\mathcal{N}^{2}$, where the angular dependence was accounted for in the harmonic decomposition. This

allows us to use relations that hold for 2-dimensional manifolds in further simplifications. One particularly useful is the ability to reduce the derivatives in the gravitational sector by one, introducing a variable Ω defined as:

$$\nabla_{[a}v_{b]} = r^{-4}\Omega\varepsilon_{ab}. \tag{3.1.21}$$

Now, we define $\tau_a = \tilde{\rho}_a - r^2\mathcal{T}v_a$ in terms of the matter variable. Taking the gradient of the odd equation $\varepsilon^{ab}\nabla_a O_a = \varepsilon^{ab}\nabla_a\Upsilon_b$ yields:

$$r^2\nabla_a(r^{-2}\nabla^a\Omega) - \frac{\lambda^2-2}{r^2}\Omega = r^2\varepsilon^{ab}(\nabla_a\tau_b + \nabla_a\Upsilon_b). \tag{3.1.22}$$

Defining $\Omega = r\Psi$ we get these two covariant equations for the odd sector:

$$r^2\nabla_a(r^{-2}\nabla^a r\Psi) - \frac{\lambda^2-2}{r^2}r\Psi = r^2\varepsilon^{ab}(\nabla_a\tau_b + \nabla_a\Upsilon_b) \tag{3.1.23}$$

$$\nabla_a(r^2v^a) - \tilde{\rho} = \Upsilon. \tag{3.1.24}$$

These equations are fully general as long as the background metric has spherical symmetry, and they allow us to choose a matter content for the energy-momentum tensor, such as electromagnetism or a null dust solution, as will be in our case. Once we chose a background solution for that matter content, we can use these equations to obtain perturbation equations for that spacetime. Now, we will focus on a static spacetime to see how its perturbation equations behave and what information they hold. After that, we will focus on the main topic of the thesis, namely, characterizing how the properties of a static spacetime change under a mass change of its central object.

3.2 Quasinormal modes and the solutions to the master equations

In this section, we will introduce the physical assumptions that should be considered while solving the master wave equation for black holes, leading us to the definition of quasinormal modes. This analysis closely follows [11] and will give us insight in solutions to modes of oscillations of a BH and all other contributions it possesses. To enforce the ideas of this chapter, we will consider a general Master equation for a static spherically-symmetric spacetime, which has the form [11]:

$$\frac{d^2\Psi_s}{dr_*^2} + (\omega^2 - V_s)\Psi_s = 0, \tag{3.2.1}$$

where Ψ_s is the Master variable for a perturbation field of spin s, r_* is the tortoise coordinate, ω are the eigen-frequencies of the system, and V_s is the potential corresponding to an axial or polar sector, also differing for fields of different spin [11]. Physical properties of our system come as appropriate boundary conditions at the event horizon and future null infinity. Since nothing can escape the event horizon or approach us from infinity, these boundary conditions will give rise to a dissipative effect. Most systems in this analysis have $V_s = 0$ as we approach the horizon ($r_* \to -\infty$), and since noting can escape the horizon, only ingoing modes should

be present:

$$\Psi \sim e^{-i\omega(t+r_*)}, \quad r_* \to -\infty (r \to r_+). \tag{3.2.2}$$

At infinity, for asymptotically flat spacetime (with are the ones considered in this project) the master variable should only have outgoing solutions:

$$\Psi \sim e^{-i\omega(t-r_*)}, \quad r \to \infty. \tag{3.2.3}$$

Due to the dissipate nature of our system and the fact that there is an ambiguity regarding the time at which each mode is excited, amplitude contributions of each mode are hard to estimate. This, among other things [11], points to the conclusion that it is not possible to expand our solutions as a sum of QNMs [4,11]. With the dissipation effect in mind, it naturally follows that the eigen-frequencies of our system will have a real and imaginary part. The real part holds the information about the frequency of oscillations, while the imaginary part is the inverse damping time [11]. These solutions are then sorted by their overtone number n, where the fundamental mode $n = 0$ is the longest lived mode, with each overtone being more damped, leading to the fundamental mode dominating the ringdown waveform [11]. Since quasinormal frequencies do not depend on the source or the way the black hole was perturbed, they hold information about fundamental properties of the black hole they correspond to [11], such as mass, spin and charge. This fact gives a strong reason for studying this phenomena, since a good grasp on the properties of QNFs and a rigorous way of calculating them can give us a complete set of information about a black hole they are sourced from (based on the no-hair theorem of BHs). The stage where the QNMs dominate the ringdown is interpreted as a relaxation of the black hole through the leakage from the light-ring, making the light-ring integral when determining properties of the source of QNMs [11]. As we saw in section 2.2.2, the light-ring is not so well defined for a mass-changing black hole, but our model will provide evidence that the source is still guided by the properties of the "instantaneous" light-ring at each timestep.

3.2.1 QNMs as the poles of a Green's function

There exists a systematic approach that gives rise to QNMs of our system, which also gives insight to other contributions to the wave solution of the perturbation equations. This approach consists of constructing a solution to the perturbation equation using the Green's function technique [4, 11]. To achieve this, we first need to take the Laplace transform of the equation and then apply the Green's function technique to the equation [4]. We will first go trough an example on a closed system with a known analytical solution, and then translate the approach to our problem.

Pedagogical example: vibrating string To illustrate the techniques that we are going to use to describe the behavior of a gravitational wave equation and its solutions, we will first go through a simple example that encapsulates the main features of the technique [18]. To do so, we start with a general form of a differential equation governing a vibrating string (setting the

speed of the wave to $c = 1$ and and restricting the domain of of x to $0 \leq x \leq \pi$):

$$\frac{\partial^2 u}{\partial x^2} - \frac{\partial^2 u}{\partial t^2} + V(x)u = \mathcal{S}. \tag{3.2.4}$$

First step in the approach requires taking a Laplace transform, which is in general:

$$\mathcal{L}u(t,x) \equiv \hat{u}(\omega, x) = \int_{t_0}^{\infty} u(t,x)e^{i\omega t}dt. \tag{3.2.5}$$

The original function is, in terms of Laplace transform:

$$u(t,x) = \frac{1}{2\pi}\int_{-\infty+ic}^{\infty+ic} \hat{u}(\omega, x)e^{-i\omega t}d\omega. \tag{3.2.6}$$

Using this, the Laplace transformation of (3.2.4) leads to:

$$\frac{\partial^2 \hat{u}}{\partial x^2} + \left[\omega^2 + V(x)\right]\hat{u} = I(\omega, x), \tag{3.2.7}$$

with:

$$\mathcal{L}\left[\frac{\partial^2 u}{\partial t^2}\right] = \int_{t_0}^{\infty} \frac{\partial^2 u}{\partial t^2}e^{i\omega t}dt = -\omega^2\hat{u} - e^{i\omega t_0}\left[i\omega u(t,x) - \frac{\partial u(t,x)}{\partial t}\right]_{t=t_0}, \tag{3.2.8}$$

where the source term consists of the Laplace transform of the original source plus the terms involving information about initial conditions:

$$I(\omega, x) = e^{i\omega t_0}\left[i\omega u(t,x) - \frac{\partial u(t,x)}{\partial t}\right]_{t=t_0} + \hat{\mathcal{S}}. \tag{3.2.9}$$

With this, we reduced our PDE to ODE, and since we have a source term (even without the presence of $\hat{S}$), we can employ the Green's function technique for solving differential equations [33]. The Green's function is constructed such that:

$$\left[\frac{\partial^2}{\partial x^2} + \left[\omega^2 + V(x)\right]\right] G(x, x') = \delta(x - x'), \tag{3.2.10}$$

and the technique tells us that a particular solution is simply given by:

$$\hat{u} = \int I(\omega, x')G(x, x')dx', \tag{3.2.11}$$

where the homogeneous solutions are used to construct the Green's function. To get to the original solution, an inverse Laplace transform has to be taken, yielding:

$$u(t,x) = \frac{1}{2\pi}\int dx' d\omega I(\omega, x')G(x, x')e^{-i\omega t}. \tag{3.2.12}$$

Having the outline of the technique, the next steps would be:

- construct the Green's function for the differential operator in question based on the boundary conditions
- find a Laplace transform of the source

- integrate to get the full solution

There is a general way to construct a Green's function [33]. First, find two independent solution to the homogeneous equation, each one satisfying one of the boundary conditions. Find the Wronskian, which is the measure of how independent the two homogeneous solutions are:

$$W(\omega, r) = \hat{u}_1 \hat{u}_2' - \hat{u}_1' \hat{u}_2. \tag{3.2.13}$$

The Green's function is then given by:

$$G(x, x', \omega) = \begin{cases} \frac{\hat{u}_1(x)\hat{u}_2(x')}{W(\omega,x)} & \text{for } x \leq x' \\ \frac{\hat{u}_1(x')\hat{u}_2(x)}{W(\omega,x)} & \text{for } x \geq x' \end{cases}. \tag{3.2.14}$$

In the case of the string, the two independent solution are $\hat{u}_1 = \sin(\omega x)$ and $\hat{u}_2 = \sin(\omega(x - \pi))$ and the Wronskian $W(\omega) = -\omega \sin(\omega\pi)$. In this example, we see that the Wronskian is constant with respect to x, which in general is not true[2]. Once we have the Green's function, we can perform the integration over ω. In the case of the string, the poles of the Green's function are going to be the zeros of the Wronskian [18]. Since we know the Wronskian for the vibrating string, with its zeros being on the real axis, the full solution can be calculated using the Cauchy's residue theorem, and subtracting the additional contribution from the half circle:

$$\int f(\omega) d\omega = \int_{HC} f(\omega) d\omega - \oint f(\omega) d\omega, \tag{3.2.15}$$

$$\oint f(\omega) d\omega = 2\pi i \sum_n Res(f(\omega), \omega_n). \tag{3.2.16}$$

The solution is then given by:

$$\begin{aligned} u(t, x) = \frac{1}{2\pi} \int_{HC} d\omega \int dx' I(\omega, x') G(x, x') e^{-i\omega t} \\ - i \int dx' \sum_n Res(I(\omega, x') G(x, x') e^{-i\omega t}, \omega_n). \end{aligned} \tag{3.2.17}$$

Taking the real part of the solution and setting $\hat{\mathcal{S}} = t_0 = V(x) = 0$, we reproduce the well known equations for the free vibrating string:

$$u(t, x) = \sum_{n=1}^{\infty} \left(\bar{C}_n \cos nt + \bar{C}_n' \sin nt \right) \sin(nx), \tag{3.2.18}$$

where $\bar{C}_n$ and $\bar{C}_n'$ can be extracted by the usual way of applying completeness relations of trigonometric functions.

[2] as we will see in the case of BH perturbation equation, but we will still be able to go around this

Master equation for GWs To investigate the differential equation governing gravitational waves, we take the same steps as in the vibrating string case. The differential equation we will use to calculate the quasinormal modes takes a general form:

$$\frac{\partial^2 R(v,r)}{\partial r^2} + p(r)\frac{\partial^2 R(v,r)}{\partial v \partial r} + q(r)R(v,r) = \mathcal{S}(v,r). \tag{3.2.19}$$

As in the example of a vibrating string, we start with taking the Laplace transform of the Master equation:

$$\frac{\partial^2 \hat{R}(\omega,r)}{\partial r^2} - i\omega p(r)\frac{\partial \hat{R}(\omega,r)}{\partial r} + q(r)\hat{R}(\omega,r) = I(\omega,r), \tag{3.2.20}$$

where:

$$I(\omega,r) = \hat{\mathcal{S}} + p(r)e^{i\omega v_0}R(v_0,r). \tag{3.2.21}$$

The Green's function for this differential equation satisfies:

$$\left[\frac{\partial^2}{\partial r^2} - i\omega p(r)\frac{\partial}{\partial r} + q(r)\right] G(r,r',\omega) = \delta(r-r'), \tag{3.2.22}$$

and with it, the particular solution to the original equation is:

$$R(v,r) = \int d\omega dx' I(\omega,r')G(r,r',\omega)e^{-i\omega v}. \tag{3.2.23}$$

To separate the integral into its contributions, we need to know the poles of the Green's function. Since we don't have a specific solution for the $G(r,r',\omega)$, we can take the known behavior of Green's functions of GW equations [11], represented in Figure 3.1. There are an infinite number of poles of the Green's function, where the first few are represented. These poles come in pairs, where the real part of QNMs have the same absolute value. The branch cut along $-\mathrm{Im}(\omega)$ is also highlighted along the contour we take to integrate this function.

Analyzing the contributions based on this, a general function takes the form:

$$\begin{aligned}\int_{-\infty+ic}^{\infty+ic} f(\omega)d\omega = &-\oint f(\omega)d\omega + \int_0^{-i\infty}(f(\omega+\epsilon)-f(\omega-\epsilon))d\omega \\ &+ \int_{2QC} f(\omega)d\omega + \oint_{ES} f(\omega)d\omega,\end{aligned} \tag{3.2.24}$$

$$\oint f(\omega)d\omega = 2\pi i\sum_n Res(f(\omega),\omega_n), \tag{3.2.25}$$

where $2QC$ represents two semicircles extending to $\mathrm{Im}(\omega)\to-\infty$ and ES represents the

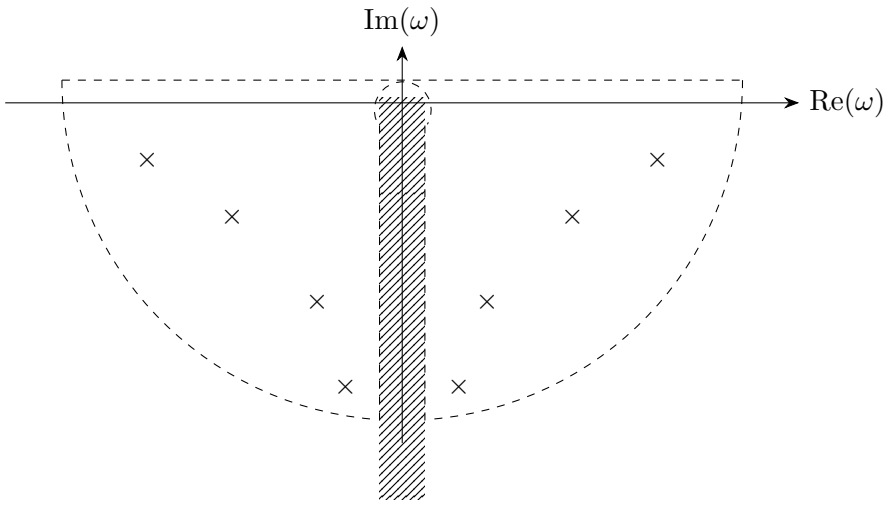

Figure 3.1: Diagram representing the integration contour over ω for equation (3.2.23). A first few poles of the Green's function are represented alongside the branch cut that goes from $\omega = 0$ extending to $\mathrm{Im}(\omega) \to -\infty$.

circle around zero. Using this, (3.2.23) becomes:

$$R(w,r) = \frac{1}{2\pi}\int dx' \Bigg[-2\pi i \sum_n Res(I(\omega,r')G(r,r',\omega)e^{-i\omega w},\omega_n) \tag{3.2.26}$$

$$+ \int_{2QC} I(\omega,r')G(r,r',\omega)e^{-i\omega w} \tag{3.2.27}$$

$$+ \int_{ES} I(\omega,r')G(r,r',\omega)e^{-i\omega w} \tag{3.2.28}$$

$$+ \int_0^{-i\infty} \Big(I(\omega+\epsilon,r')G(r,r',\omega+\epsilon)e^{-(i\omega+\epsilon)w} \tag{3.2.29}$$

$$- I(\omega-\epsilon,r')G(r,r',\omega-\epsilon)e^{-(i\omega-\epsilon)w} \Big) d\omega \Bigg], \tag{3.2.30}$$

where the 4 contributions represent [4]:

- The first contribution (3.2.26) are the poles of the Green's function (without the essential singularity), corresponding to QNMs.
- The last one (3.2.29)-(3.2.30) is the contribution of the branch cut, representing late-time decay tails.
- Leaver [4] argues that (3.2.27) "It is 2QC that propagates the high frequency response, and which reduces to the free-space Green's function in the limit as the mass of the black hole goes to zero.", which is interpreted as the prompt response.
- there are some new ideas that the contribution from the essential singularity (3.2.28) are actually the ones contributing to the prompt response.

We will see all these contributions in Section 4.2.3 when solving the Master equation numerically, but since the mass change of the black hole gives the most interesting phenomena during the

quasinormal ringing, we will explore only this contribution going forward. From the example for the vibrating string, we saw that it is crucial to have a constant Wronskian if we want to interpret the QNMs as the poles of the Green's function (or zeros of the Wronskian). Since equation (3.2.19) does not possess this property, we can take the following steps to get a constant Wronskian (and transform it to an equation of the form (3.2.1)). First, using master equation in EF coordinates for this example, we can make a transformation as follows:
Define a new $R(r) = g(r)f(r)$, giving the Wronskian:

$$W(r,\omega) = ce^{-\int p(r)dr} = c\frac{re^{2ir\omega+i(2\omega+i)\log(1-r)}}{g(r)^2}. \tag{3.2.31}$$

Now, for a constant Wronskian $g(r)$ has to be:

$$g(r) = e^{i\omega(r+\log(r-1))}\sqrt{\frac{r}{r-1}}, \tag{3.2.32}$$

and the new wave equation is:

$$\left(\frac{(l+1)l}{r} + \frac{r^2\omega^2}{r-1} - \frac{15}{4(r-1)r^2} + \frac{4}{(r-1)r}\right) f(r) + (r-1)f''(r) = I(\omega,r)e^{-i\omega(r+\log(r-1))}\sqrt{\frac{r-1}{r}}. \tag{3.2.33}$$

We see that indeed this equation is of the form (3.2.1), leading us to switch the attention to its solutions, essentially to match what has been done in previous reviews discussing this [11]. There are two independent solutions for the homogeneous part of the equation (3.2.1) corresponding to the two boundary conditions, one at the horizon and one at infinity, Ψ_{r_+} and Ψ_{∞_+}, respectively [4]. The solution at the horizon should have the following asymptotic behaviors:

$$\lim_{r\to r_+} \Psi_{r_+} \sim e^{-i\omega r_*}, \tag{3.2.34}$$

$$\lim_{r\to\infty} \Psi_{r_+} \sim A_{in}(\omega)e^{-i\omega r_*} + A_{out}(\omega)e^{i\omega r_*}, \tag{3.2.35}$$

with the solution at the infinity having the behavior:

$$\lim_{r\to\infty} \Psi_{\infty_+} \sim e^{i\omega r_*}, \tag{3.2.36}$$

$$\lim_{r\to r_+} \Psi_{\infty_+} \sim B_{in}(\omega)e^{i\omega r_*} + B_{out}(\omega)e^{-i\omega r_*}. \tag{3.2.37}$$

Considering these asymptotic behaviors of the solutions Ψ_{r_+} and Ψ_{∞_+}, we get the following Wronskian:

$$W(\omega) = 2i\omega A_{in}. \tag{3.2.38}$$

QNMs are defined so that they are the values of the frequency for which the solution at the horizon and at infinity become dependent. In other words, we want to obtain one solution that obeys both boundary conditions. This shows that QNMs can be defined as zeros of the Wronskian, or equivalently poles of the Green's function.

We end this section by finishing the analysis of the QNMs part of the solution. The full solution can be constructed as:

$$\Psi(\omega,r)=\Psi_{\infty_+}\int_{-\infty}^{r_*}\frac{I(\omega,r)\Psi_{r_+}}{2i\omega A_{\rm in}}dr'_*+\Psi_{r_+}\int_{r_*}^{\infty}\frac{I(\omega,r)\Psi_{\infty_+}}{2i\omega A_{\rm in}}dr'_*. \tag{3.2.39}$$

We can make a physical assumption that the perturbations in question are going to be observed at a distance from the source that can be approximated with infinity, which allows us to consider only the second contribution to the Master variable [34]. Quasinormal modes come in pairs, matching with the absolute value of the real part, as presented in Figure 3.1. These modes are always excited together, leading to the real part of the solution:

$$R(w,r)=-\mathrm{Re}\left[\sum_n B_n e^{-i\omega_n(t-r)}\int_{-\infty}^{\infty}\frac{I(\omega,r)\Psi_{r_+}}{A_{\rm out}}dr\right], \tag{3.2.40}$$

where:

$$B_n=i\frac{A_{out}}{W(\omega)}=\frac{A_{out}}{2\omega A_{in}}. \tag{3.2.41}$$

The usual approach is to expand A_{in} around a quasinormal mode frequency as follows:

$$A_{in}=(\omega-\omega_n)\left(\frac{dA_{in}}{d\omega}\right)\Bigg|_{\omega=\omega_n}, \tag{3.2.42}$$

leading to:

$$B_n\equiv\frac{A_{out}}{2\omega}\left(\frac{dA_{in}}{d\omega}\right)^{-1}\Bigg|_{\omega=\omega_n}. \tag{3.2.43}$$

We notice that B_n's only depends on the background geometry, making them a valuable quantity in analysis of black hole ringing [11]. When supplemented with initial conditions, we get the whole amplitude C_n of the QNM contribution to the perturbation in question.

3.3 Quasinormal modes of a static black hole

In this section, we will go through the technique of calculating the QNMs of a static black hole. This technique of solving for QNMs was introduced by Leaver [3]. We will consider the perturbation equation in advanced EF coordinates:

$$ds^2=-\left(1-\frac{2M}{r}\right)dv^2+2dvdr+r^2d\Omega^2. \tag{3.3.1}$$

Using this line element in the covariant Master equation (3.1.23) and setting the matter perturbations to zero $\tau_b=\Upsilon_b=0$, we arrive to the following perturbation equation for a static black hole in EF coordinates:

$$\begin{aligned}&\left(\frac{-l(l+1)}{r}+\frac{6M}{r^2}\right)\mathcal{R}(v,r)+\frac{2M}{r}\mathcal{R}_{,r}(v,r)\\&-2r\mathcal{R}_{,vr}(v,r)+(r-2M)\mathcal{R}_{,rr}(v,r)=0.\end{aligned} \tag{3.3.2}$$

Since we concluded that the scale of the system is set by the mass of the black hole (if $G = c = 1$), we can set $M = 1/2$ without loss of generality, and describe its impact on the QNMs after calculating them. To separate the time coordinate v we use the ansatz:

$$\Psi_l(v, r) = e^{-i\omega v} R_{\omega l}(r). \tag{3.3.3}$$

Inserting this ansatz into the perturbation equation (3.3.2) we get the equation for the radial part of the perturbation:

$$\left(\frac{-l(l+1)}{r} + \frac{3}{r^2}\right) R_{\omega l}(r) + \frac{1}{r} R_{\omega l,r}(r) - 2ri\omega R_{\omega l,r}(r) + (r-1) R_{\omega l,rr}(r) = 0, \tag{3.3.4}$$

which translates to the Schwarzschild coordinates used in Leavers paper by rescaling EF gravitational variable by $e^{i\omega r}(r-1)^{i\omega}$. This equation has two regular singularities at $r = 0$ and $r = 1$, with an additional irregular singularity at $r = \infty$. This type of equation belongs to the class of singly confluent Heun equations [35]. If we inspect the asymptotic behavior of solutions, we arrive to one regular and one irregular solution at the horizon, and two wave solutions at infinity (recaling (3.3.3) and $v = t + r$):

$$\lim_{r \to r_+} R_{\omega l} \sim \begin{cases} 1, & \text{regular} \\ (r-1)^{2i\omega}, & \text{irregular} \end{cases}, \tag{3.3.5}$$

$$\lim_{r \to \infty} R_{\omega l} \sim \begin{cases} 1, & \text{ingoing} \\ e^{2i\omega r}, & \text{outgoing} \end{cases}. \tag{3.3.6}$$

Because of this, two local solutions, one regular and one irregular, can be constructed around the regular singularity at the horizon, represented by Heun functions [35]:

$$R^I_{\omega l}(r; 1) = r^3 HeunC(2i\omega, -2i\omega, 4, -2\omega^2, 4 - l(l+1) + 2\omega^2, 1 - r), \tag{3.3.7}$$

$$R^{II}_{\omega l}(r; 1) = r^3 (r-1)^{2i\omega} HeunC(2i\omega, 2i\omega, 4, -2\omega^2, 4 - l(l+1) + 2\omega^2, 1 - r), \tag{3.3.8}$$

where $R^I_{\omega l}$ represents in-going waves at the horizon, and $R^{II}_{\omega l}(r; 1)$ represents outging waves. Around the irregular singularity at infinity, one can construct Thomé solutions [35]:

$$R^I_{\omega l}(r; \infty) = e^{2i\omega(r + \log(r))} \sum_{k=0}^{\infty} \rho_k(\omega, \ell) r^{-k}, \tag{3.3.9}$$

$$R^{II}_{\omega l}(r; \infty) = \sum_{k=0}^{\infty} \sigma_k(\omega, \ell) r^{-k}, \tag{3.3.10}$$

where again, $R^I_{\omega l}(r; \infty)$ represents the waves going into the singularity, and $R^{II}_{\omega l}(r; \infty)$ propagating away from the singularity. Once we have the local solutions, the next step would be to continue these solutions analytically, with the goal of having a valid solution for the entire domain. See [35] for details. The final result for the radial part of the master variable $\mathcal{R}(v, r)$

can be expressed as (with the appropriate boundary conditions at the horizon and infinity):

$$R_{\omega l}(r) = e^{2i\omega(r-1+log(r))}\sum_{k=0}^{\infty} a_k(\omega,\ell)\frac{(r-1)^k}{r^k}. \tag{3.3.11}$$

With this solution, we go to the radial equation (3.3.4) (which needs to be multiplied through with r for this to work) with the goal of getting the three term recurrence relation as in [3] and with it, obtaining the continued fraction needed for calculating the QNMs. The three term recurrence relation has the form:

$$\alpha_0 a_0 + \beta_0 a_0 = 0, \tag{3.3.12}$$

$$\alpha_n a_{n+1} + \beta_n a_n + \gamma_n a_{n-1} = 0, \quad n = 1, 2, \ldots, \tag{3.3.13}$$

where we can set a_0=1. The coefficients α_n, β_n and γ_n are function of ω, ℓ and n:

$$\alpha_n = (n+1)(n-2i\omega+1), \tag{3.3.14}$$

$$\beta_n = -l^2 - l - 2n^2 - 2n(1-4i\omega) + 8\omega^2 + 4i\omega + 3, \tag{3.3.15}$$

$$\gamma_n = n^2 - 4in\omega - 4\omega^2 - 4. \tag{3.3.16}$$

The sum (3.3.13) converges only for the values of ω that correspond to quasinormal modes. When this is satisfied, it is said that for $n \to \infty$, a_n form a minimal solution of (3.3.13). Now, the ratio of of successive a_n will be given by a continued fraction:

$$\frac{a_{n+1}}{a_n} = \cfrac{-\gamma_{n+1}}{\beta_{n+1} - \cfrac{\alpha_{n+1}\gamma_{n+2}}{\beta_{n+2} - \cfrac{\alpha_{n+2}\gamma_{n+3}}{\beta_{n+3} - \cdots}}} = \frac{-\gamma_{n+1}}{\beta_{n+1}-}\frac{\alpha_{n+1}\gamma_{n+2}}{\beta_{n+2}-}\frac{\alpha_{n+2}\gamma_{n+3}}{\beta_{n+3}-}\ldots. \tag{3.3.17}$$

Evaluating (3.3.17) for $n = 0$ and using (3.3.12) we obtain the following conditions:

$$\frac{a_1}{a_0} = -\frac{\beta_0}{\alpha_0}, \tag{3.3.18}$$

$$\frac{a_1}{a_0} = \frac{\gamma_1}{\beta_1-}\frac{\alpha_1\gamma_2}{\beta_2-}\frac{\alpha_2\gamma_3}{\beta_3-}\ldots. \tag{3.3.19}$$

Equating these two expressions we arrive to the characteristic equation for the quasinormal modes ω_n:

$$0 = \beta_0 - \frac{\alpha_0\gamma_1}{\beta_1-}\frac{\alpha_1\gamma_2}{\beta_2-}\frac{\alpha_2\gamma_3}{\beta_3-}\ldots. \tag{3.3.20}$$

A root finding algorithm can be used to solve this implicit equation for $\omega_n = \omega_R + i\omega_I$. We extract the fundamental mode $n = 0$ for different values of ℓ, presented in Table 3.3.1. Since the mass M is the only scale we have in our problem, we can conclude that the quasinormal

ℓ	$M\omega_R$	$M\omega_I$	ℓ	$M\omega_R$	$M\omega_I$
2	0.373672	0.088962	14	2.773224	0.096037
4	0.809178	0.094164	15	2.966795	0.096060
8	1.606194	0.095671	16	3.160229	0.096080
10	1.996788	0.095864	17	3.353550	0.096096
11	2.191334	0.095925	18	3.546776	0.096110
12	2.385541	0.095971	19	3.739923	0.096121
13	2.579487	0.096008	20	3.933001	0.096131

Table 3.3.1: Values of the QNM fundamental mode for different values of ℓ. These values are identified as $\omega_0(\ell)$.

modes are related to the mass as (since $[\omega] = 1/L$):

$$M\omega = \omega_0(n, \ell) = \omega_0(0, \ell) = \omega_0(\ell), \tag{3.3.21}$$

$$M(\omega_R + i\omega_I) = \omega_{0R}(\ell) + i\omega_{0I}(\ell), \tag{3.3.22}$$

where $\omega_0(\ell)$ is the constant relating the mass and the frequency ($\omega_0(0) = 0.373672$), representing the black hole signature. We are only going to consider the fundamental mode $n = 0$, so we omit the explicit dependence on it.

We can observe that the real part of the frequency changes it's value when increasing ℓ, but the imaginary part changes a bit in the low ℓ region and slows down for large ℓ. This is a well known behavior of quasinormal modes in the eikonal limit, $\ell \gg 1$, where the expression for the qusinormal modes obtains the form [36]:

$$\omega_{nl} \approx (l + 1/2)\Omega - i\gamma_L(n + 1/2), \tag{3.3.23}$$

where Ω is the Keplerian frequency of the circular photon orbit, and γ_L is the Lyapunov exponent of the orbit [19].

As we saw, the quasinormal frequencies are dependent on the scale of the system, governed by the mass of the black hole. This further motivates us to explore what will happen to QNMs if this scale changes through the process of emission of QNMs. Any differences from the equations valid in the static case can lead us to new insights about black hole dynamics and the influence on the fundamental properties of the governing spacetime.

4 Relaxation of a mass-changing black hole

We now turn to a spacetime that can model a mass-changing black hole. There are different models describing a mass-changing black hole and pointing to its importance, but they are all quite complicated and sometimes require going to third order perturbation theory to capture this effects [23]. The model used in this project is comparably simple and allows the description of this phenomena even at first order, with the constraint of restricting ourselves to spherically symmetric accretion. The spacetime in question is called Vaidya spacetime and it describes a so called *pure radiation field*, or *null dust* solution to Einstein filed equations [32]. It was first introduced by Vaidya to study the spacetime around a radiating star [24]. This spacetime is

asymptotically flat, spherically symmetric and describes an eikonal approximation to a radial flow of unpolarized radiation.

Vaidya spacetime can be used to model multiple physical processes regarding black holes. For some, Vaidya spacetime can be quite an accurate model, while for others it can be a good first order approximation. One such physical scenario is a well-studied ringdown of a merger of two black holes [8]. Vaidya spacetime can describe processes right after the merger, where part of the energy is lost due to emission of gravitational waves, while the rest of the energy goes back to the remnant black hole, incensing its mass. Ringdown of a remnant black hole is usually described by perturbation equations for a static black hole, where the final mass is fixed throughout the relaxation process [8]. This does not necessarily have to (and probably does not) hold, motivating the exploration of effects induced by the part of the energy that accretes back to the remnant black hole. Another process is a black hole stationed in an astrophysical environment [22], with spherical symmetry restricting us a bit. A well known black holes with accretion disks, something we used to "take a picture" of a black hole [37], wouldn't fit the category of Vaidya spacetime, but it would still provide an insight to its non-stationary processes. Also, in the case of a black hole losing mass, it can model Hawking radiation [38]. Analysis of perturbation equations of the Vaidya metric can probe into all these physical scenarios and much more, motivating its study.

This spacetime has previously been studied with the goal of extraction of its QNMs [25, 26], with a generalization to charged black holes and analysis of scalar and electromagnetic perturbations. In [26], they identified the inertial behavior of quasinormal modes, while [25] showed that the peak of inertial behavior should be more prominent for more abrupt changes. In this project, we will expand on this by trying to capture this interplay between dynamics of the background with the non-adiabatic properties of QNMs, leading us to a systematic description of this phenomena. A similar approach is taken for extraction of frequencies as in [25].

We will start by introducing the spacetime and casting it into a coordinate representation. This will lead us, through analysis of Einstein filed equations, to differential equations governing this spacetime. We will then impose asymptotic conditions that will allow us to interpret these coordinates in a physical way. After that, we will focus on perturbation equations of this spacetime and acquire an odd sector equation describing gravitational perturbations. Once we have the perturbation equations and equations governing the spacetime, we will focus on the numerical approach for solving them. Having this algorithm, we will be able to consider a wide range of accretion processes and extract information from the properties of its gravitational waves and the background they live in. Using the methods described above, we will be able to capture the non-adiabatic behavior, allowing us to create a model that describes this behavior systematically. Once these results are obtained, we will explore how to create a unified description of this behavior for many different accretion processes. One of the main results will be the description of the non-adiabatic behavior for different ℓ modes, pointing to a general behavior of high ℓ.

4.1 Vaidya spacetime and its perturbation equations

In this section, we will introduce the Vaidya spacetime, cast it into double-null coordinates and from the Einstein filed equations obtain the differential equations governing the dynamics of this spacetime. We will also discuss physical assumptions and asymptotic conditions that we would like to impose on this spacetime. In the end, we will derive the odd sector perturbation equation, governing dynamics that we are interested in.

4.1.1 Vaidya spacetime

Vaidya spacetime was first introduced by Vaidya in 1951. [24]. This kind of spacetime is obtained by promoting the energy-momentum tensor in Schwartzchild spacetime $T_{\mu\nu} = 0$ to an energy-momentum tensor of a pure radiation field, satisfying the following Einstein filed equations:

$$G_{\mu\nu} = \Phi K_\mu K_\nu, \;\; K^\mu K_\mu = 0, \tag{4.1.1}$$

where $G_{\mu\nu}$ is a spherically symmetric Einstein tensor, and K^μ and Φ are a vector and a function. Consequence of (4.1.1) is that the energy momentum tensor is conserved and K^μ is a geodesic, which can be chosen to be affinely parametrized as:

$$K^\mu \nabla K^\nu = 0. \tag{4.1.2}$$

Physically, this is a spacetime describing the high frequency (eikonal) approximation to unpolarized radiation, with energy density Φ, propagating along the null direction K^μ. We already saw one coordinate representation of this spacetime in section 2.2.2, where we used extended Eddington Finkelstein coordinates obtained by promoting the constant mass to a mass as a function of the advanced time v. In this section, we will switch to another set of coordinates, called double-null coordinates (u, v, θ, ϕ), which are more suitable for numerical simulations. Penrose diagram of the Vaidya spacetime in double-null coordinates is presented in Figure 4.1. It shows the grid used in simulations, the infall of null-matter and initial conditions used in the evolution of the algorithm.

4.1.2 Double-null coordinates

Double null coordinates are defined with the following line element:

$$ds^2 = -2f(u, v)dudv + r^2(u, v)d\Omega^2, \tag{4.1.3}$$

where $r(u, v)$ is the area radius and $d\Omega^2$ is a metric of a 2-sphere. The coordinates remain well defined while $f(u, v) \neq 0$. K^μ can be taken to point in one of the null direction, and up to rescalings of K^μ Eq. (4.1.2) fixes

$$K = \frac{1}{f(u, v)}\partial_u. \tag{4.1.4}$$

Next, we focus on the Einstein filed equations of Vaidya spacetime in double null coordinates, which are derived in Appendix B.

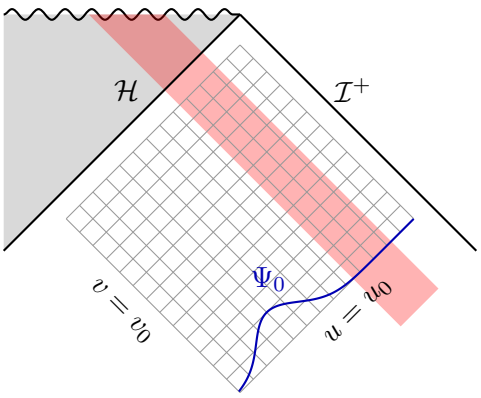

Figure 4.1: Penrose diagram describing Vaidya spacetime. Values $\{u_0, v_0\}$ represents the region where we impose initial conditions, represented by a blue curve. The end of the grid $\{u_{max}, v_{max}\}$ represents how close we get to the horizon and infinity, respectively. Red shaded region represents the infall of null matter, influencing the position of the horizon and the light-ring.

The main results from this analysis are the following equtions:

$$\partial_v r = -\varepsilon\left(1 - \frac{2m(v)}{r}\right), \quad \varepsilon = \frac{f(u,v)}{2\partial_u r}, \tag{4.1.5}$$

$$\Phi = -4\varepsilon\frac{\partial_v m(v)}{r^2} = 2\frac{|\partial_v m(v)|}{r^2}, \tag{4.1.6}$$

with the mass function $m(v)$ defined in the following way:

$$m(v) = \frac{1}{2}r^3 R^{\theta\phi}{}_{\theta\phi} = \frac{r}{2f}(f + 2\partial_u r\partial_v r). \tag{4.1.7}$$

A few words need to be said about these equations. First, we notice that these equations hold information about the transport of $r(u,v)$ along the v direction, and once the initial condition $r(u,v_0)$ is prescribed, there exists a unique solution to (4.1.5). Next, we notice that the equation for Φ automatically implies the weak-energy condition. In our analysis we restrict to solutions with $f(u,v) > 0$ and the time orientation of K^μ is going to be fixed so it is future-oriented. Then, the area-radius function varies according to:

$$K^\mu\nabla_\mu r = 2\varepsilon. \tag{4.1.8}$$

This implies that for $\varepsilon > 0$ or $\varepsilon < 0$ the profiles of $m(v)$ correspond to out-going or in-going pure radiation fields, respectively. We will consider multiple mass profiles that obey:

$$m(v \to \pm\infty) = \begin{cases} m_2 \\ m_1 \end{cases}. \tag{4.1.9}$$

Lastly, we need to choose an asymptotic condition for the flow equation (4.1.5) of $r(u,v)$. We do it as follows, at a slice $v = v_{max}$ where v_{max} is taken so the condition:

$$\left|\frac{m_2 - m(v_{max})}{m_2}\right| \ll 1, \tag{4.1.10}$$

is achieved, we demand:

$$r(u, v_{max}) = \frac{m_2 - m_1}{|m_2 - m_1|} \frac{v_{max} - u}{2} - 2m(v_{max}) \ln \left| \frac{r(u, v_{max})}{2m(v_{max})} - 1 \right|. \tag{4.1.11}$$

This choice is quite important if we want to have the same physical intuition of these coordinates as it is already established in other coordinates describing spherically symmetric spacetimes. This choice allows us to interpret (u, v), for large v, as the retarded and advanced times (reminiscent of the ones in EF coordinates) corresponding to asymptotics state of Vaidya spacetime. With this choice, the future event horizon and future null infinity are located at $u \to \infty$ and $v \to \infty$, respectively. One thing worth to note is that for solutions $r(u, v)$, $f(u, v)$, Φ, K... with an increasing mass profile corresponding to in-going pure-radiation solution, there is an out-going pure-radiation solution $\tilde{r}(u, v) \equiv r(-u, -v)$ with a decreasing mass profile $\tilde{m} \equiv m(-v)$.

4.1.3 Perturbation equations

To obtain perturbation equation for the odd sector for the Vaidya spacetime (4.1.1), parametrized by the coordinates (4.1.3), we start by substituting (where we omit the subscript ℓ for brevity):

$$\Upsilon_b = 0, \quad \tau_b = \tilde{\rho}_a = \Phi K_a \tilde{v}, \quad v^a = \frac{j^a}{r^2}, \quad \tilde{\rho}^L = \tilde{\theta}^L = \tilde{\sigma}^L = 0, \tag{4.1.12}$$

which come from the gauge invariant formalism applied to Vaidya spacetime [25]. This reduces the general odd sector covariant Master equation (3.1.24) and the EM conservation (3.1.23):

$$r^2 \nabla_a \left(r^{-2} \nabla^a (r\Psi) \right) - \frac{\lambda^2 - 2}{r} \Psi = r^2 \epsilon^{ab} K_b \nabla_a (\Phi \tilde{v}), \tag{4.1.13}$$

$$K^a \nabla_a \left(r^2 \Phi \tilde{v} \right) = 0, \quad \nabla_a j^a = 0. \tag{4.1.14}$$

Solving for $\tilde{v}$ in the first equation of (4.1.14) gives an exact solution [25]:

$$\tilde{v} = \frac{F(v)}{r^2 \Phi}, \tag{4.1.15}$$

where $F(v)$ is a free function of v, corresponding to initial conditions for $\tilde{v}$. Having the solution for $\tilde{v}$, we can turn to the covariant perturbation equation (4.1.13). Equations governing the spacetime are going to be of great help in simplifying the solution:

$$\partial_v r = -\varepsilon \left(1 - \frac{2m(v)}{r} \right), \quad \partial_u r = 2\varepsilon f(u, v), \quad \partial^2_{uv} r = -\frac{m(v) f(u, v)}{r^2}, \tag{4.1.16}$$

since we are able to substitute any derivatives of $r(u, v)$ with these expressions. This analysis (presented in Appendix C) leads us to the following Master equation for the Vaidya spacetime in double-null coordinates [30]:

$$\left(\partial^2_{uv} - \frac{f}{r} \left(\frac{3m(v)}{r^2} - \frac{(\ell(\ell+1)}{2r} \right) \right) \Psi = \frac{2f}{r^2} \varepsilon F(v). \tag{4.1.17}$$

Inspecting this equation, we see that gravitational and matter fluctuations decouple. As can be deduced from numerical solutions presented in [25], non-zero $F(v)$ doesn't excite QNMs in a somewhat predictable manner. Since we are interested in QNMs and extraction of properties of the black hole based on them, we will set $F(v) = 0$ for the remainder of this project. This looses a bit of generality, but is a perfectly allowed choice. We can also observe that with $F(v) = 0$ and $m(v) = const.$, we recover the extensively studied Regge-Wheeler equation, proving the consistency of the derived Master equation.

4.2 Solving the perturbation equations: numerical results

In this section, we will describe an algorithm for solving equations (4.1.5) and (4.1.17), yielding us a numerical solution for the Master variable $\Psi(u, v)$. Once we obtain this, we will investigate these solutions on a generic example with a goal of gaining a better intuition of this spacetime. After that, we will introduce the extraction process of the QNMs from these solutions, comment on the generic results we obtain from it and quantify its precision. Once we have performed these calculations for many different accretion processes, we will be able to investigate these solutions and draw conclusions from their properties.

4.2.1 Numerical framework

Having the Master equation (4.1.17), we can turn to methods of solving it. The solutions are going to be acquired on a finite grid $[u_0, u_{max}] \times [v_0, v_{max}]$ with the grid resolution of $\Delta_u = \Delta_v = 0.1m_1$. On this grid, we need to numerically integrate the Master equation of the form:

$$\partial^2_{uv}\Psi + V(u, v)\Psi = 0, \tag{4.2.1}$$

where

$$V(u, v) = -\frac{f(u, v)}{r(u, v)}\left(\frac{3m(v)}{r(u, v)^2} - \frac{(\ell(\ell + 1)}{2r(u, v)}\right). \tag{4.2.2}$$

To calculate of $V(u, v)$, we need to solve for $r(u, v)$ and $f(u, v)$ using equations (4.1.5). We start with $r(u, v)$, where we have to impose the condition (4.1.11). Since this condition has to also be solved for $r(u, v_{max})$ we can employ a root-finding algorithm to extract it's value. This generally works when $r_* = (v - u)/2$ is large, and needs a different approach when $r_* \lesssim 0$. We are going to focus on the root-finding algorithm, which gives good solutions for $r(u, v)$ outside the event horizon, which is the region we are considering. Once we have $r(u, v_{max})$, we use it as initial conditions in the first order finite difference method for obtaining $r(u, v)$. Having $r(u, v)$, we solve the second equation in (4.1.5) using forth order finite difference method to obtain $f(u, v)$. With these solutions, we have all the building blocks for $V(u, v)$. We now turn to evolving the full master equation (4.2.1) using the usual characteristic algorithm [25,39]. The initial conditions are set by by assuming that $v = v_0$ surface is located far enough, so we can set $\Psi(u, v_0) = 0$. On the $u = u_0$ surface, we impose a Gaussian initial conditions:

$$\Psi(u_0, v) = \Psi_0 \exp\left(-\frac{(v - v_\Psi)^2}{\sigma^2_\Psi}\right). \tag{4.2.3}$$

With this, the time update for the wave equation is given by:

$$\Psi_N = \Psi_E + \Psi_W - \Psi_S - \frac{\Delta_u \Delta_v}{2} V_S (\Psi_W + \Psi_E). \tag{4.2.4}$$

This algorithm will give us the values of the Master variable $\Psi(u, v)$ on the full grid. Once we have this solution, we will extract it near the horizon, labeled $\Psi_{\mathcal{H}} \sim \Psi(u_{max}, v)$ and near spatial infinity $\Psi^+_{\mathcal{I}} \sim \Psi(u, v_{max})$. This algorithm is tested on the Schwartzchild solution, with the solutions quite accurately representing the $n = 0$ modes of oscillation, with the expected convergence when increasing the resolution. Numerical algorithms were implemented in Mathematica [40], and all the plots were generated within it. The text in the plots was styled using MaTeX [41].

4.2.2 Solution of the Master equation and general properties

Once we have an algorithm to solve for $r(u, v)$, $f(u, v)$, $V(u, v)$ and $\Psi(u, v)$, we can inspect some of their properties. To do this, we still need to define a mass profile. We will mainly use a mass profile of the form:

$$m(v) = m_1 + \frac{m_2 - m_1}{2} \left(1 + \tanh\left(\frac{v - v_1}{\tau}\right) \right). \tag{4.2.5}$$

This mass profile allows us to model many different accretion scenarios, from slow and adiabatic increase to very sudden changes, controlled by the parameter τ. In addition to this mass profile, we will consider two additional ones (linear and parabolic), with the goal of generalizing the results to a wider range of accretion processes. For the sake of this section, we will set $m_1 = 1$, $m_2 = 1.5m_1, 3m_1$ and $\tau = 5m_1, 10m_1, 20m_1$.

We start our inspection with $V(u, v)$, represented in Figure 4.2. We can see that the peak of the potential is on the diagonal represented by a $u - v$ line, but not exactly on $u - v = 0$. After the mass change, this line is $(u-v)_{m_1} < (u-v)_{m_2}$, supporting the fact that the maximum of the potential is dependent on $m(v)$. Since $r_* = (u - v)/2$, we can conclude that it is acting as $r_* \propto m(v)$, which loosely represents the light-ring. Next, we can observe that the maximum of $V(u, v)$ has a smaller value for larger mass, and it is not as sharp as for smaller masses. Furthermore, we can see that as ℓ grows, the maximum of the potential also grows. Since ω_R grows with increasing ℓ, and decreases with increasing mass, we can infer a relationship between the maximum value of the potential with the value of ω_R being $V_{max} \uparrow \Rightarrow \omega_R \uparrow$. So, next to the intuition of bigger circle (light-ring)$\rightarrow$ lower frequency, we also see that the maximum value of the potential plays a role in the value of the real part of QNMs. This is actually a well know result for the WKB analysis of this phenomena [11]. Having an intuition on the behavior of our spacetime based on the potential, we turn to inspecting the effect of the mass change on $r(u, v)$. As we can see from Figure 4.3, the behavior of $r(u, v)$ is quite different based on inspecting it inside or outside of the peak of the potential. Inside, the function is approximately constant except in the region where the mass change ours. We conclude that in the region $(v - u) \lesssim 0$, $r(u, v) \approx 2M(v)$, which is the position of the event horizon. Outside of the light-ring, it grows as $r(u, v) \sim (u - v)$.

Potential $V(u,v)$ on a $u \times v$ grid for different ℓ's

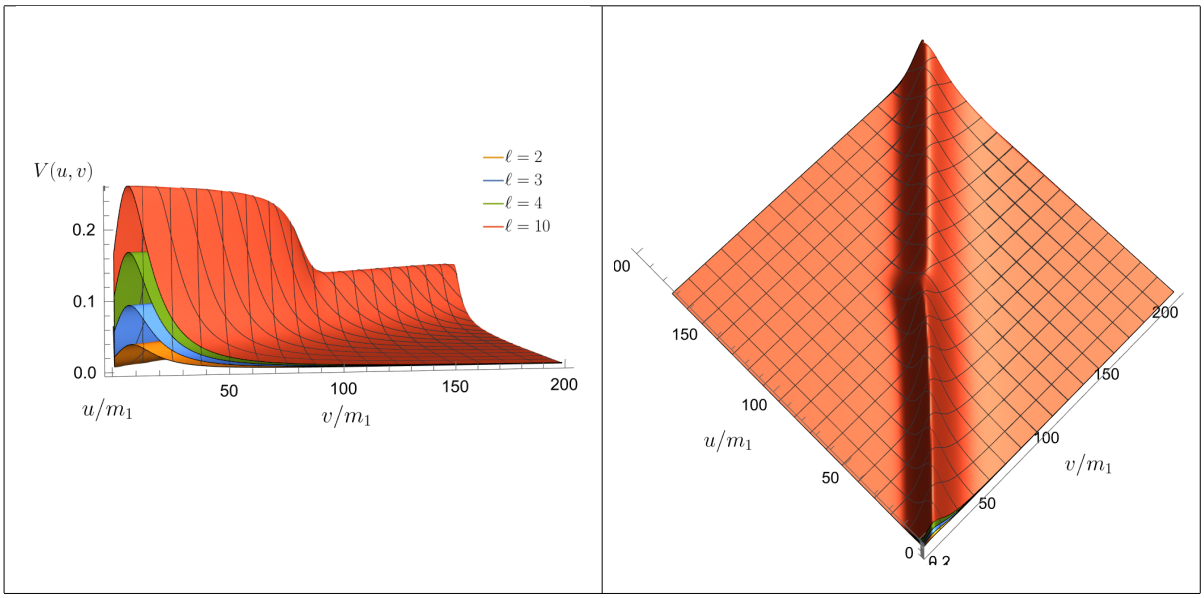

Figure 4.2: Potential $V(u,v)$ for different ℓ values. The mass profile is chosen to be (4.2.5), with parameters $m_2 = 1.5\,m_1$, $v_1 = 100m_1$, and $\tau = 5m_1$. Visual inspection of the left panel shows that the peak of the potential is related to the mass as $m(v) \uparrow \Rightarrow V_{\max} \downarrow$, and to ℓ as $\ell \uparrow \Rightarrow V_{\max} \uparrow$. The right panel shows how the position of the maximum responds to the mass change.

Area-radius $r(u,v)$ ploted on a $u \times v$ grid

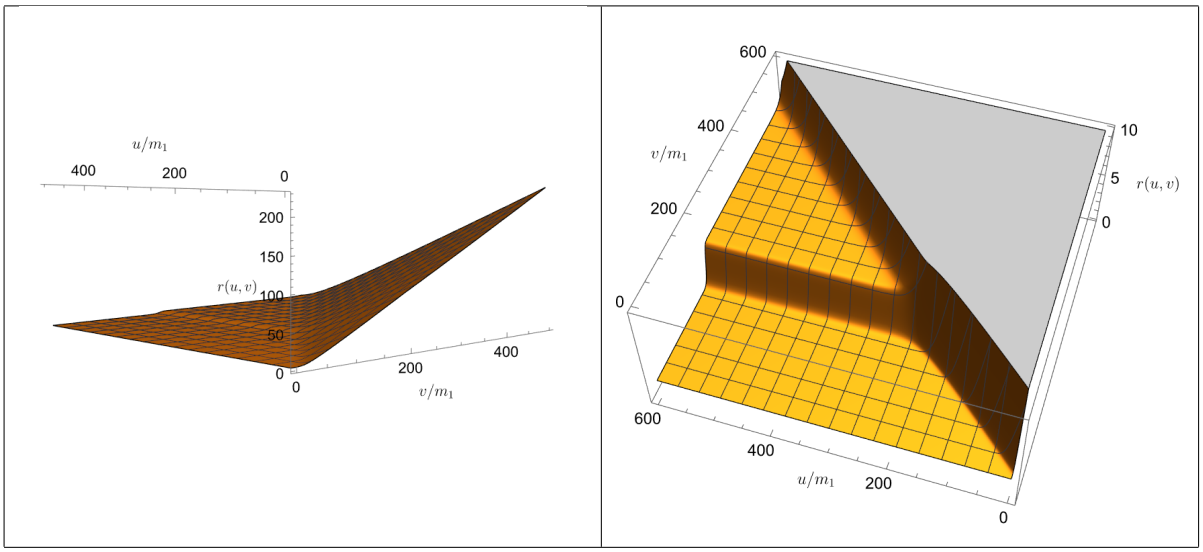

Figure 4.3: Area radius on a $u \times v$ grid, emphasizing its different behavior outside (left) and inside (right) the light-ring. The mass profile is chosen to be (4.2.5) with $m_1 = 1$, $m_2 = 3m_1$, $v_1 = 100m_1$ and $\tau = 5m_1$. Value of $r(u,v)$ inside the light-ring is $\approx 2M(v)$, matching with the position of the horizon.

Furthermore, we also consider plots of the Master variable on a $u \times v$ grid. The raw plot is presented in Figure 4.4. As we can see, the initial perturbation travels along u to some $u - v$ line, there it interacts and excites some oscillatory behavior. To closely inspect this, we can plot this function on a log plot, and add a representation of the potential $V(u,v)$, scaled so it

Plot of $\Psi(u, v)$ on a $u \times v$ grid

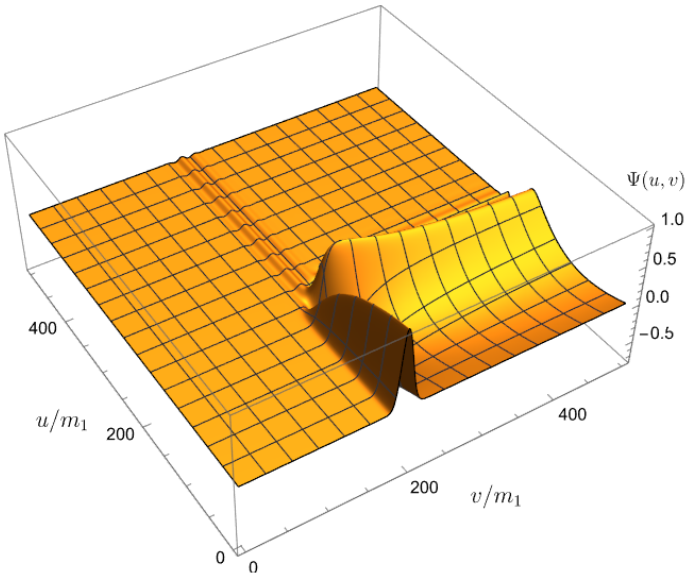

Figure 4.4: Original solution to the Master variable on a $u \times v$ grid showing the initial perturbation (4.2.3) with $\Psi_0 = 1$, $\sigma_\Psi = 2.5$ and $v_\Psi = 200$. This plot highlights the propagation of the initial data and its influence on excitations of QNMs.

highlights the interaction between the perturbation and the potential. As shown in Figure 4.5,

Log plot of $\Psi(u, v)$ on a $u \times v$ grid compared to $V(u, v)$

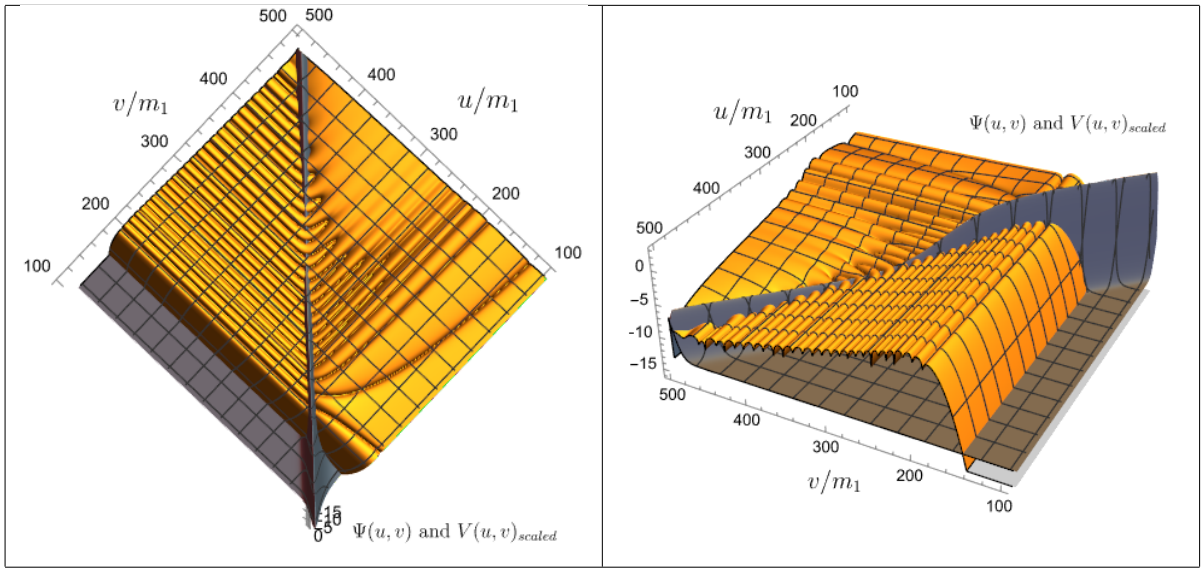

Figure 4.5: Master variable on a log plot, compared to the rescaled potential, highlighting the source of the QNMs. Initial perturbation used is (4.2.3) with $\Psi_0 = 1$, $\sigma_\Psi = 2.5$ and $v_\Psi = 200$. The mass profile is chosen to be (4.2.5) with $m_1 = 1$, $m_2 = 1.5m_1$, $v_1 = 300$ and $\tau = 10$.

the perturbation travels uninterrupted to the peak of the potential. There, it excites QNMs, with different behavior traveling towards the horizon and spatial infinity, with the source of this difference being a sligtly different behavior of the potential on each side of the peak, as described below. Reaching the point of the mass change, the source of the QNMs shifts with the peak of the potential, strongly indicating that it is indeed the source of QNMs.

We can now summarize the conclusions we made based on these plots, having in mind the processes connected to the QNMs. First, we saw different contributions to the ringdown dominating with different intensity at the horizon and spatial infinity, reflecting the different behavior of the potential on each side of its maximum, also present for a static black hole. Next, we see that there is quite a different behavior of $r(u, v)$ based on the position with respect to the peak of the potential, indicating there might be a difference imprinted in the QNMs themselves, not just in relative contributions to the ringdown waveform. Lastly, this analysis pointed to the fact that the source of QNMs is the peak of the potential, as they overlap even in a dynamical spacetime.

4.2.3 Master variable at the horizon and infinity and its QNMs

Once we have inspected the solutions to the Einstein filed equations for Vaidya spacetime and the corresponding Master equation, we can turn to analysis of its QNMs. This analysis will give us further insight to the properties of the spacetime and show us how to pick consistent reference for the non-adiabatic effects induced by the mass change.

We start by inspecting the Master variable extracted at the horizon and at spatial infinity, which are presented in Figure 4.6. First, we can notice different behaviors of the Master variable progressing through time, starting with an excitation, followed by a damped oscillatory behavior, and in the end a tail prevailing. These are exactly the contributions obtained by the Green's function technique discussed in Section 3.2. Furthermore, we can see that at the horizon, the quasinormal part of the ringdown dominates through the whole region of interest, while in the spatial infinity side, we reach the late-time tails in finite time. This is due to the different behavior of the potential, where on the spatial infinity side we have a gradual decrease of the potential, while on the horizon side we have an abrupt fall of the potential to zero. This is also present in the static case, presenting some consistency checks on this theory.

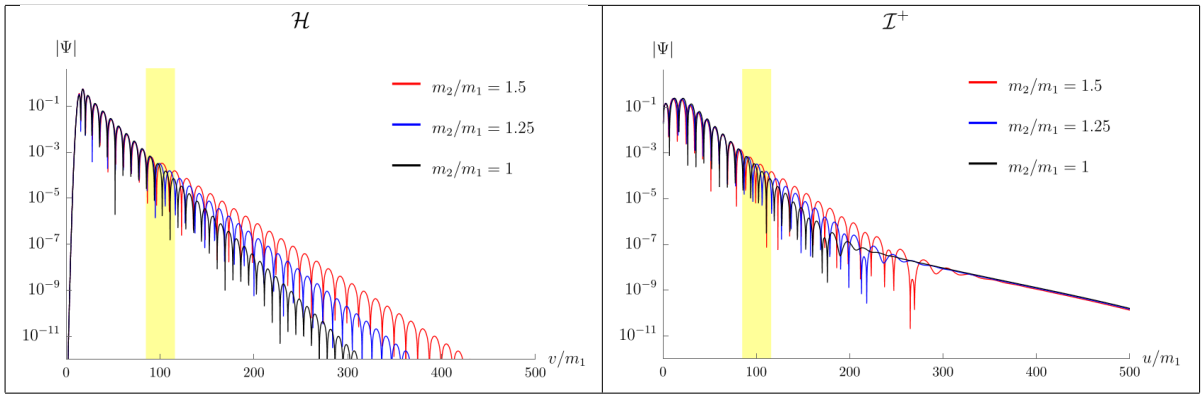

Figure 4.6: Master variable for the quadrupole mode $\ell = 2$ extracted at the horizon (left) and at infinity (right). Mass profile is chosen to be (4.2.5) with $v_1 = 100m_1$ and $\tau = 5m_1$. Highlighted region represents the time period in which the mass change happens. Visual inspection confirms that indeed as $m \to m_{1,2}$ the relationship $m(v)\omega(v) = \omega_0(\ell)$ guides the QNMs, having a lower frequency and slower decay after the accretion.

Next, we can observe the impact of a mass change during the QNM ringing. Before the mass change, all three examples match, while after the mass change we get a lower frequency

and a longer decay time for the mass-changing cases, as expected from $m(v)\omega(v) = \omega_0(\ell)$. This relationship between m and ω will prove to be true for $m \to m_{1,2}$ [25], with a different behavior in the transient.

Once we have the solutions for the Master variable at the horizon and spatial infinity, we can start extracting the QNMs from them. To do so, we employ an algorithm that identifies the positions on the grid of maximums of Abs(Ψ) and zero-crossings of Ψ, M_i and Z_i, respectively. Based on these values, we can calculate the "instantaneous" frequency and the decay rate of our wave. They are calculated as:

$$\omega_{Ri} = \frac{2\pi}{(I_{i+2} - I_i)\Delta_{u,v}}, \quad I_i = M_i, Z_i, \tag{4.2.6}$$

$$\omega_{Ii} = -\frac{\log(\Psi(M_{i+2})) - \log(\Psi(M_i))}{(M_{i+2} - M_i)\Delta_{u,v}}. \tag{4.2.7}$$

This extraction algorithm is tested on multiple toy models, proving its accuracy. Once we have these values, we can plot them against $m(v)\omega(v) = \omega_0(\ell)$, and for now, visually inspect the deviations from it. We show the values of $\omega(v)$ extracted from $\Psi_{\mathcal{H}}$ in Figure 4.7 and from $\Psi_{\mathcal{I}^+}$ in Figure 4.8, compared to $\omega_0(\ell)/m(v)$.

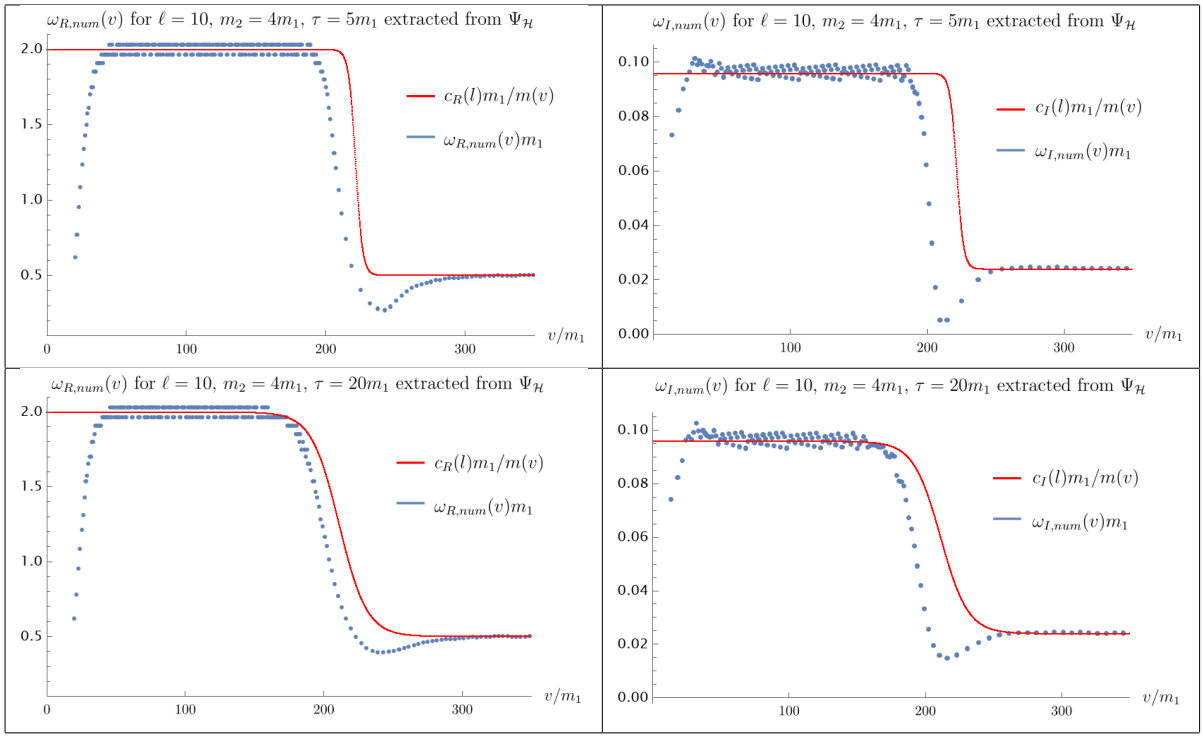

Figure 4.7: Extracted frequency $\omega_{R,\text{num}}(v)$ (left) and inverse damping time $\omega_{I,\text{num}}(v)$ (right) for the Master variable at the horizon $\Psi_{\mathcal{H}}$, plotted against $\omega_0(\ell)/m(v)$, representing a curve of adiabatic behavior. We see that as $m \to m_{1,2}$ the relationship $m(v)\omega(v) = \omega_0(\ell)$ holds (minus numerical error), but in the transient region we have lower values of the QNFs than the adiabatic curve.

For the values extracted at the horizon, in regions $m \to m_{1,2}$, we have a very good agreement with $m(v)\omega(v) = \omega_0(\ell)$ up to the resolution mentioned below. Deviations from the values in

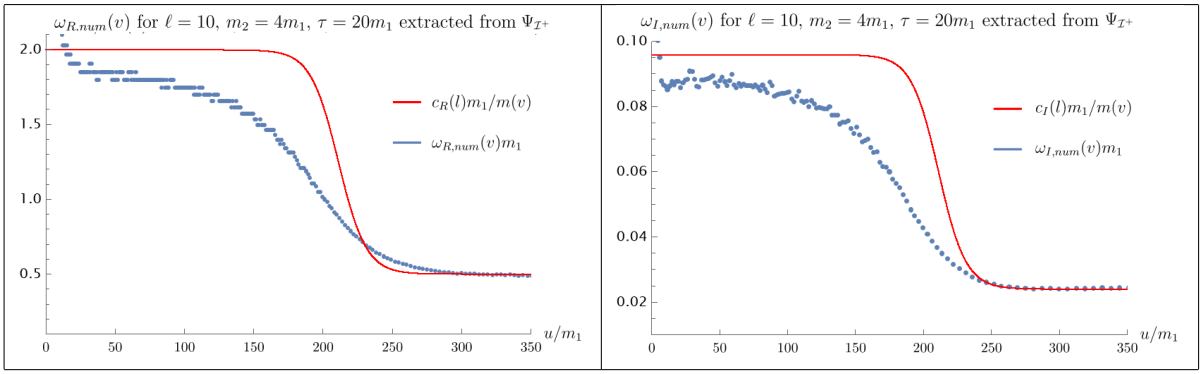

Figure 4.8: Extracted frequency $\omega_{R,\text{num}}(v)$ and inverse damping time $\omega_{I,\text{num}}(v)$ for the Master variable at infinity $\Psi_{\mathcal{I}^+}$, plotted against $\omega_0(\ell)/m(v)$, representing a curve of adiabatic behavior. We see that $m(v)\omega(v) = \omega_0(\ell)$ holds only for $m \to m_2$ and that there is no clear reference for measuring non-adiabaticity.

Table 3.3.1 can also be minimized by taking larger intervals of M_i and Z_i. This is avoided because it negatively affects the extraction of values in the transient region, which is the one of interest to us. In contrast to the agreement for $m \to m_{1,2}$, we see a significant disagreement in the transient region, where the frequency is lower than that given by $m(v)\omega(v) = \omega_0(\ell)$.

QNMs extracted at infinity have a quite different behavior, with $m(v)\omega(v) = \omega_0(\ell)$ obeyed only for $m \to m_2$. This behavior is still to be examined, with one approach pointing to a close connection with the value of V_{max}.

Since there is a clearer way to characterize the non-adiabatic behavior from the QNMs extracted at the horizon, we will focus on these for the rest of the project. In these considerations, we will have a minimum frequency extending below the $\omega_2 = \omega_0(\ell)/m_2$ value, capturing this inertial behavior. Since the frequency extraction algorithm gives some uncertainty in positioning (in time) the extracted frequencies to match the mass change, we will focus on this minimum value, and analyze its difference from $\omega_2 = \omega_0(\ell)/m_2$:

$$\Delta\omega = \omega_{min} - \omega_0(\ell)/m_2, \tag{4.2.8}$$

$$\Delta\omega_R + i\Delta\omega_I = [\omega_{R,min} - \omega_{0R}(\ell)/m_2] + i[\omega_{I,min} - \omega_{0I}(\ell))/m_2], \tag{4.2.9}$$

where ω_{min} is the minimum value of the numerically extracted frequency. We have now constructed an object $\Delta\omega$ that will measure how non-adiabatic the effects are. If its value is higher, the non-adiabatic effect is bigger.

Lastly, we comment on the resolution of the algorithm for extracting QNFs (4.2.6). This is presented in Figure 4.9. As shown, the worst discrepancy will occur for high frequency, which for us is achieved for $\ell = 20$ and $m_1 = 1$, where $\omega_R m_1 \approx 3.9330$. However, since we will extract the relevant values at m_2, and since in most of the analysis $m_2 = 4m_1$ (one of the reasons for that choice), the deviation from the real value is at most what is represented by the red line in the plot.

Also worth a mention is a tug of war between the extraction algorithm and the sampling of the transient region. Logically, more times we extract the value in the transient region, more precisely we catch the behavior of the QNFs. This would correspond to higher frequency of

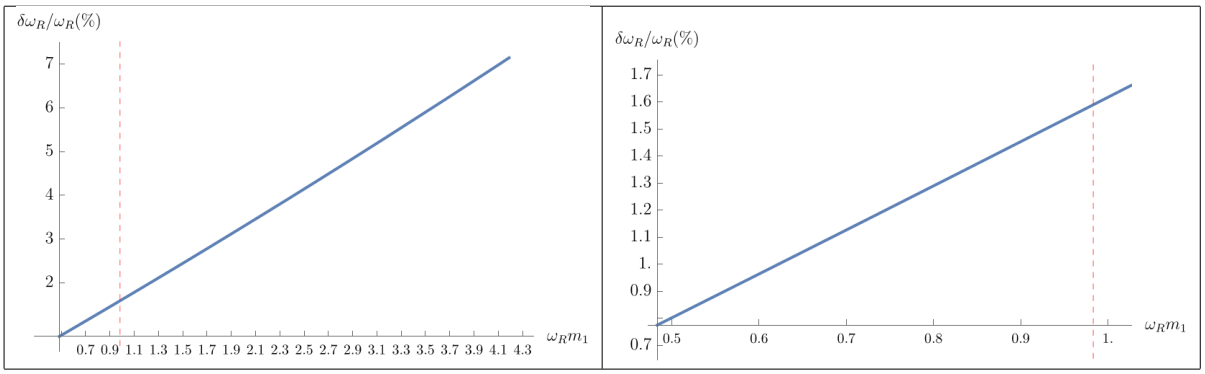

Figure 4.9: Resolution of the algorithm for extraction of the real part of QNFs (left) and a zoomed in version (right). $\ell = 20$ and $m_1 = 1$ case, where $\omega_R m_1 \approx 3.9330$, represents the highest error in our algorithm. Red line represents $\omega_0(20)/4m_1$, which will be the highest error of the main results since all other considerations have a lower frequency.

oscillation, since we extract only at maximums and zero-crossings. But, as we see from Figure 4.9, higher the frequency, larger the error. This can be mitigated by increasing the resolution of the grid $\Delta_{u,v}$, or by applying some other algorithm for extraction of frequencies, both shown to be intangible for this project.

4.3 Characterization of the non-stationary behavior: analysis of numerical results

We now turn to a qualitative description of non-stationary behavior of a mass-changing black hole. We will attempt to describe this quantitatively, since we will see some regularities pointing to a possible normalization. But, this kind of description is hidden in a numerical approach as this one, since there is an ambiguity of choosing the proper normalization.

We will start by introducing the key features of the non-stationary behavior of the QNMs for a mass-changing black hole. Once we have the idea of this behavior, the main focus will shift to the non-adiabatic properties for different ℓ modes going though different durations of accretion. The rate of accretion is going to be captured by $(dm/dv)_{max}$, which holds the information about the maximum rate of mass change and is proportional to how dynamical the spacetime is. This analysis will show a general behavior for high ℓ, allowing us to model it systematically. After that, we will see how this behavior can be generalized to different parameters of the background and shown that $\Delta\omega$ has the same functional form in all these cases. This will allow us to propose a general model that describes the connection between the non-adiabatic effects in QNMs and the dynamics of the spacetime.

For the sake of introducing this phenomena, we will use the mass profile (4.2.5), fix m_1, m_2, ℓ, and vary τ. Once we have $\Delta\omega$ as defined in (4.2.8) for many different τ's, we can plot them against $(dm/dv)_{max} \sim (m_2 - m_1)/[\sim$ time of change$]$. We see that this choice is dimensionless and that it grows for a more dynamical spacetime, nicely characterizing the dynamical behavior induced by a mass change. This choice is scale independent, raising some potential problems. But, as we will discover when analyzing the behavior for different m_2, if we started with $1/[\sim$ time of change$]$ (or $(d^2m/dv^2)_{max}$), we would still end up with this result, as

it is a choice that generalizes this behavior. The generic results showing the connection between the non-adiabatic behavior and the dynamics of the spacetime are shown in figure 4.10. As it

Behavior of $\Delta\omega_R$ for different $(dm/dv)_{max}$

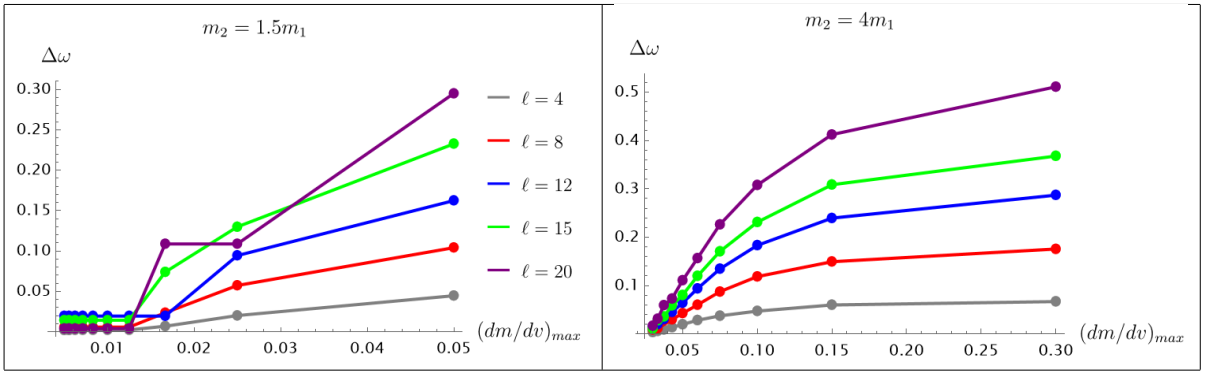

Figure 4.10: $\Delta\omega_R$ plotted against $(dm/dv)_{max}$ for $m_2 = 1.5m_1$ (left) and $m_2 = 4m_1$ (right). We use the same τ's for both of these plots. We can see that for $m_2 = 1.5m_1$ we are reaching the adiabatic behavior, but not for $m_2 = 4m_1$. This is expected because $m_2 = 4m_1$ is a more abrupt change, not allowing the spacetime to relax in that time frame.

can be seen, there is a range of $(dm/dv)_{max}$ where $\Delta\omega = \omega_{num} - \omega_0(\ell)/m_2 \approx const.$, which we can identify with an adiabatic region where $m(v)\omega_{num} \approx \omega_0(\ell)$. With decreasing τ, making the mass change more abrupt, we transition to a region where this discrepancy grows. We identify this as a non-adiabatic region, and this region will be of interest to us. Observing these plots, we can preliminarily conclude that the non-adiabatic effects grow with the increasing dynamics of the underlying spacetime, and that we have a similar functional dependence for different ℓ modes.

As mentioned, we will now focus on the description of this phenomena for different ℓ modes. After that, we will attempt to generalize this behavior to any m_1, m_2 and τ. We will also generalize this to any mass function that has a starting m_1, final m_2, and a transient region (such as linear growth or parabolic growth). This is made possible by the fact that $(dm/dv)_{max} \sim (m_2 - m_1)/[\sim$ time of change$]$ holds for a wide range of this types of functions. After that, we will evaluate the impact of $(dm/dv)_{max}$ on $\Delta\omega$ with the aim of gaining insight into their interplay. This will give us a guide for proposing a function that describes this dependence. We will then use this function as a base for assessing the goodness of proposed dependencies on ℓ. Finally, we will combine all the results and propose a single, universal behavior that governs non-adiabatic effects induced by a mass change of a black hole.

4.3.1 Analysis of the behavior for different ℓ's

We will now focus on the non-adiabatic properties of the modes for different ℓ's. Plots for $\Delta\omega_R$ and $\Delta\omega_I$ are presented in Figure 4.11. As we can see, the discrepancy of the real part of the QNFs grows with ℓ, while the imaginary part asymptotes to a certain value for high ℓ. This indicates that the non-adiabatic behavior might depend on the value of the QNFs, since the very QNFs behave in this way (3.3.23). Normalizing $\Delta\omega$ by $\omega_0(\ell)/m_1$ shows that this is indeed the case, and is presented in Figure 4.12. Physical process behind this could be the

Behavior of $\Delta\omega_R$ and $\Delta\omega_I$ for the same values of $(dm/dv)_{max}$

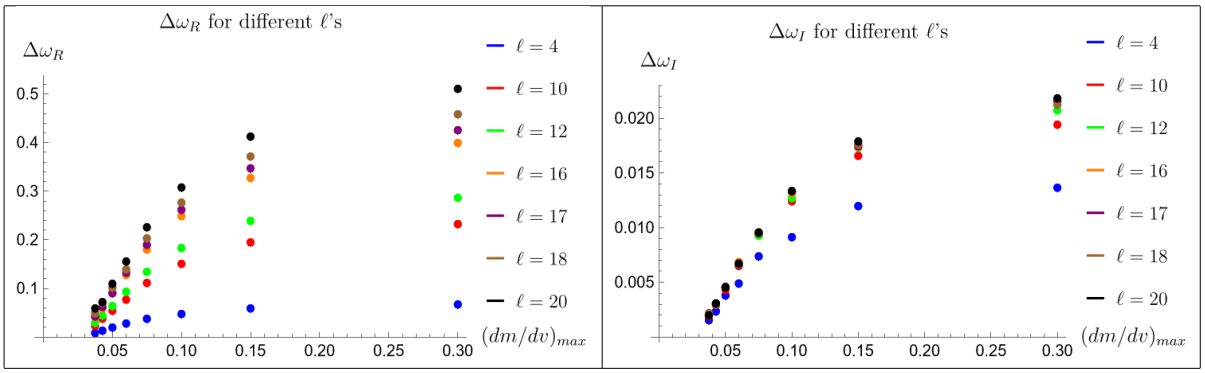

Figure 4.11: $\Delta\omega_R$ plotted against $(dm/dv)_{max}$ for $\Delta\omega_R$ (left) and $\Delta\omega_I$ (right). We use $m_2 = 4m_1$ and the same τ's for both of these plots. We can see that for $\Delta\omega_R$, the discrepancy of the real part of the QNFs grows with ℓ, while the imaginary part asymptotes to a certain value for high ℓ. This is the same behavior as the very QNFs have, pointing to their connection to $\Delta\omega$.

interplay between the timescales of the modes compared to the background. If the period of oscitation is smaller, the fractional change of the period (based on $m(v)\omega(v) = \omega_0(\ell)$) is going to be larger than for a longer period, disturbing its stationary state more appreciably. These

Behavior of $\Delta\omega_R/\omega_{0R}(\ell)$ and $\Delta\omega_I/\omega_{0I}(\ell)$ for the same values of $(dm/dv)_{max}$

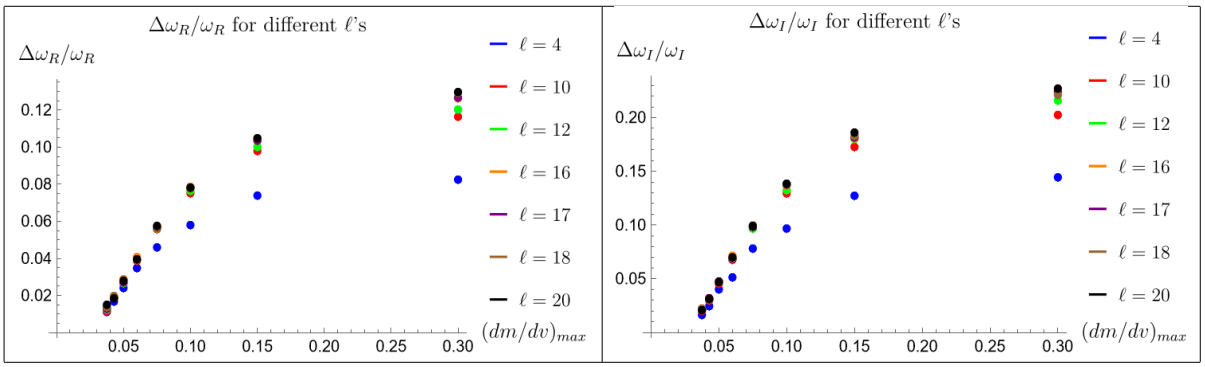

Figure 4.12: $\Delta\omega_R/\omega_{0R}(\ell)$ (left) and $\Delta\omega_I/\omega_{0I}(\ell)$ (right) plotted against against $(dm/dv)_{max}$. We use $m_2 = 4m_1$ and the same τ's for both of these plots. These plots now show us the discrepancy in percentage for the initial values of QNFs and point to a general behavior for high ℓ.

normalized plots show the discrepancy in percentage of the initial values of the QNFs. We can see that this discrepancy is higher for the imaginary part of QNFs, than for the real part by an order of $\Delta\omega_I/\omega_{0I} \approx 2\Delta\omega_R/\omega_{0R}$ for the same values of the parameters of the background. Since $\Delta\omega_R$ and $\Delta\omega_I$ seemingly have the same functional dependence and we are for now interested in the qualitative description, we will focus on $\Delta\omega_R$. This analysis leads us to the following dependence on the value of the QNFs:

$$m_1\Delta\omega \propto \omega_0(\ell) f((dm/dv)_{max}). \tag{4.3.1}$$

Furthermore, we can investigate the remaining dependence on ℓ's for low ℓ. This leads us to the following conclusion:

$$m_1\Delta\omega \propto \frac{l-1.75}{l+1/2} f\Big(\frac{l+2}{l}((dm/dv)_{max}\Big) \xrightarrow{\ell\to\infty} \frac{\omega_0(\ell)}{m_1} f((dm/dv)_{max}), \tag{4.3.2}$$

where for high ℓ we lose the explicit dependence on it, as expected. The way we obtain these and all future dependencies on the parameters of our spacetime is described in Appendix D. Described analysis was used for obtaining the functional form, where constants were physically motivated, but hand picked. Nonetheless, this shows that there is a unified behavior of non-adiabatic effects, which is a good first step in describing this phenomena. Dependence (4.3.2) has

$\Delta\omega$ plotted against $(dm/dv)_{max}$ for different ℓ's

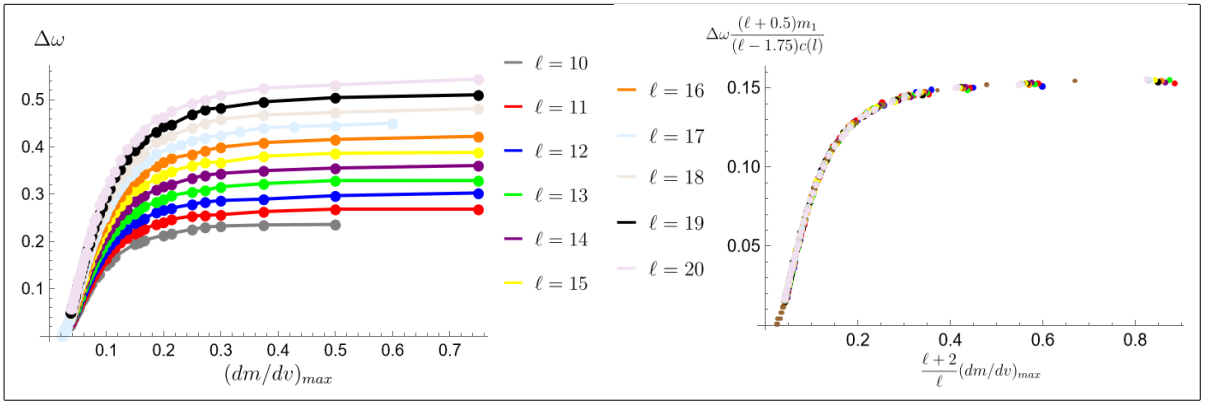

Figure 4.13: $\Delta\omega_R$ plotted against $(dm/dv)_{max}$ for different ℓ's. Mass profile is chosen to be (4.2.5). Original discrepancy $\Delta\omega$ seems to have the same functional dependence for different ℓ's (left), and it is possible to generalize this dependence as presented in (4.3.2) (right).

been shown to be a good approximation for $\ell = 8$ and higher, with lower ℓ's still having a more involved dependence. Plots showing the original data and rescaled data are shown in Figure 4.13. They support the dependence presented, but some discrepancies can still be seen. This motivates a need for numerical solutions with higher resolution, yielding more accurate results and a more precise relation. We will assess how well these proposed dependencies describe this behavior in Section 4.3.4.

4.3.2 Analysis of the behavior for different mass profiles

Considering different mass profiles, we arrive to the plot represented in Figure 4.14. As we can see, the non-adiabatic behavior still has a general functional behavior, where the difference between mass profiles is in the values of $(dm/dv)_{max}$. The relation between different mass profiles is governed by scaling the x-axis with a constant factor c_m. With this, we find a very good agreement for all the mass profiles in question. If we take the linear growth as a reference, which has exactly $(dm/dv)_{max} = (m_2 - m_1)/[\text{time of change}]$, we can see that we need to scale the x-axis of tanh mass profile by $c_m \approx 1/3$ and for the parabolic growth $c_m \approx 1.2$. This leads us to the following functional dependence, while keeping m_1, m_2 and ℓ fixed:

$$m_1\Delta\omega \propto f(c_m(dm/dv)_{max}). \tag{4.3.3}$$

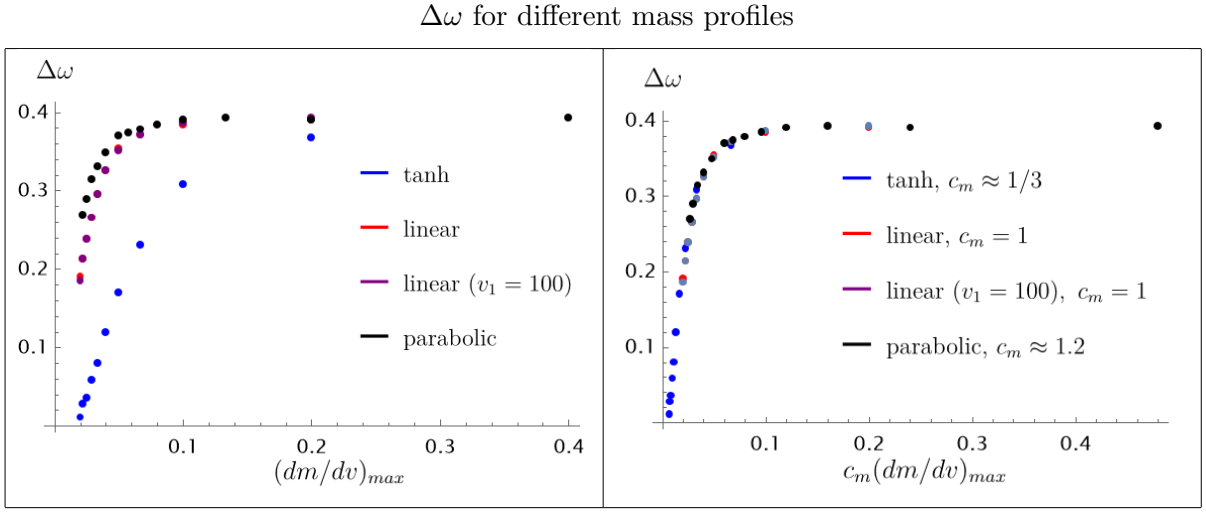

Figure 4.14: $\Delta\omega$ for different mass profiles plotted against $(dm/dv)_{max}$ (left) and against a rescaled x-axis $c_m(dm/dv)_{max}$ (right). Values for the mass profiles are $m_2 = 4m_1$ and $v_1 = 200m_1$, and the $\ell = 15$ mode is considered. In purple we can see the results for a linear mass profile with $v_1 = 100m_1$. This is to show that this phenomena does not depend on the distance between the initial perturbation and the start of accretion.

Although this seems to generalize the behavior, no general prescription was found to calculate c_m. The conclusion that should be taken from this analysis is that it is possible to generalize this behavior to different mass function (with proper care). Since we have found a general functional dependence of the $\Delta\omega$ for any reasonable mass profile, we will now focus only on the mass profile (4.2.5) where:

$$(dm/dv)_{max} = \frac{m_2 - m_1}{2\tau}. \tag{4.3.4}$$

4.3.3 Analysis of the behavior for different m_1's and m_2's

Considering that m_1 sets the scale for our problem, it comes as no surprise that all the dimensional values our problem also scale with m_1. Since $[\Delta\omega] = 1/L$, $[\tau] = L$ and $[m_2 - m_1] = L$, functional dependence extracted is then, (keeping m_2, and ℓ fixed):

$$m_1\Delta\omega \propto f\left((dm/dv)_{max} = \frac{(m_2 - m_1)}{2\tau}\frac{m_1}{m_1} = \frac{(m_2 - m_1)}{2\tau}\right). \tag{4.3.5}$$

We get a more interesting behavior when inspecting the dependence on the m_2, while keeping ℓ and m_1 fixed. We should expect the discrepancy to be higher for larger m_2 since the spacetime becomes more dynamical. On the other hand, based on $m(v)\omega(v) = \omega_0(\ell)$, higher mass should mean a lower frequency, making the discrepancy lower. As we see, the final mass of the black hole has the most involved dependence, since its influence goes both ways. Nonetheless, we managed to capture its influence, represented in the plots for different m_2 shown in Figure 4.15. As we can see, the discrepancy (4.2.8) is lower for higher m_2. This can be expected (based on $m(v)\omega(v) = \omega_0(\ell)$) because of the previously concluded fact that lower the value of the frequency, lower the discrepancy. The functional dependence for this change was a bit brute

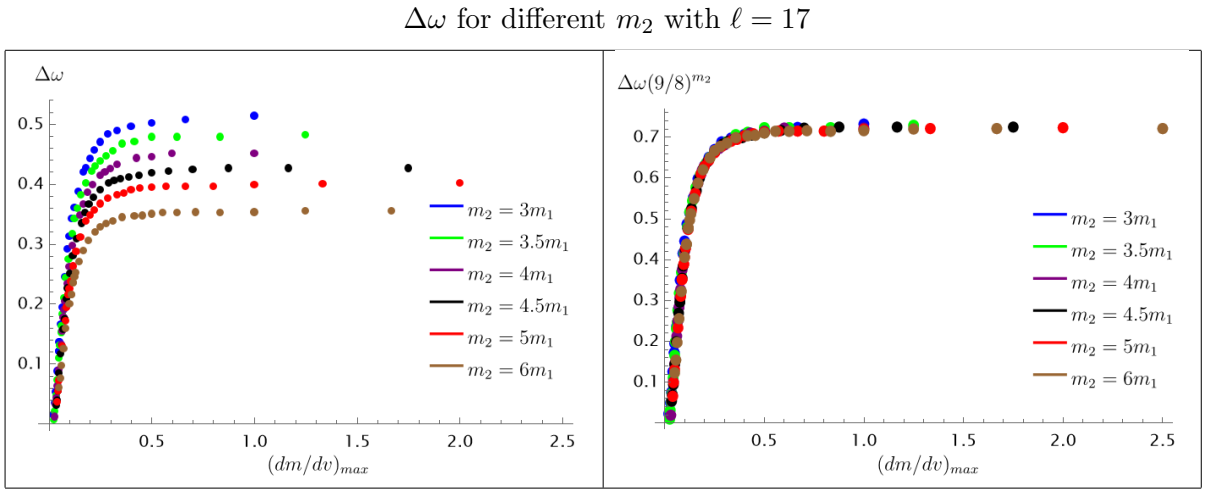

Figure 4.15: $\Delta\omega$ for different m_2 plotted against $(dm/dv)_{max}$ (left) and against a rescaled $\Delta\omega(9/8)^{m_2}$ (right). Value of the inital mass is $m_1 = 1$, and $\ell = 17$. This shows that rescaling as proposed in (4.3.6) is on the right track.

forced, but we find a very good match with the following:

$$m_1\Delta\omega \propto \left(\frac{8}{9}\right)^{\frac{m_2}{m_1}} f((dm/dv)_{max}), \tag{4.3.6}$$

where the term $(8/9)^{m_2/m_1}$ describes the influence of the value of the QNMs. Interestingly, the first derivative of the mass $(dm/dv)_{max}$ nicely catches the influence induced by the dynamics of the spacetime, by itself holding the information for generalizing this behavior for different m_2.

4.3.4 Modeling the non-adiabatic behavior and an in depth analysis of its dependence on ℓ

Previous three subsections gave us a base for building a unified model that describes the non-adiabatic effects of QNMs for a Vaidya black hole. Since we showed that $f((dm/dv)_{max})$ can describe the non-adiabtatic behavior of QNMs for a plethora of dynamical spacetimes, we can focus on finding one function $f((dm/dv)_{max})$ and then use it to investigate the proposed dependencies. We will only focus on assessing the behavior of $\Delta\omega$ for different ℓ modes to present the techniques used in the analysis.

The dependence of the non-adiabatic effect on ℓ was found to be:

$$m_1\Delta\omega \propto \omega_0(\ell)\frac{l-1.75}{l+0.5} f\Big(\frac{l+2}{l}(dm/dv)_{max}\Big), \tag{4.3.7}$$

or, for high ℓ:

$$m_1\Delta\omega \propto \omega_0(\ell) f((dm/dv)_{max}). \tag{4.3.8}$$

Inspecting the functional dependence of $\Delta\omega$ on $(dm/dv)_{max}$ from many of the figures presented in this section, we can see that the non-adiabatic effects grow for more dynamical spacetime, but at some point they gets saturated and approach a constant value. This should not be assumed beforehand, but should be expected for a physical scenario. The fact that there are

no infinities if we push this behavior to the limit is a well received property. Based on this, we can conclude that this behavior resembles an inertial behavior or a dynamical friction behavior, where the value grows with increasing rate of mass change.

Based on a physical and numerical analysis, we find that this functional dependence fits the data best:

$$f(x) = a + \frac{b}{1 + x^2/c}, \tag{4.3.9}$$

where for $x \to 0$ the function asymptotes to $f(0) = a + b$. This corresponds to $m_2 \to m_1$ or $\tau \gg 1$, so we could expect that the value $a + b$ represents the discrepancy in the adiabatic region. For $x \to \infty$ we get $f(\infty) \approx a$, corresponding to $m_2 \gg m_1$ or $\tau \ll 1$, which can describe a mass shell falling into a black hole instantaneously. This will be the asymptotic value of the discrepancy for the non-adiabatic region. The value c represents the steepness of the curve at its most active region, and adjustment to x axis we did while exploring the data proves to do just that. We should expect that the value of $a + b$ is smaller than a, since the adiabatic value of $\Delta\omega$ has to be smaller then the non-adiabatic one, making $b < 0$. If we assume that this function can explain the non-adiabatic region and its transfer to the adiabatic one, we should expect $a \geq 0$ and $a + b > 0$, making $-a \leq b < 0$. As we will see, this will not be exactly the case, proving that this function breaks at this transfer region (or that the numerical analysis presented here requires more resolution).

We will base the goodness of the fit on 4 values:

- **Relative residuals**: Fractional difference between data and predicted values $\hat{f}(x)$:

  $$\frac{f(x) - \hat{f}(x)}{f(x)},$$

  which will give us insight into the regions where the fit breaks. When it's value is 0, we have a perfect fit.

- $\mathbf{R}^2$: Measures the proportion of variance explained by the model:

  $$1 - \frac{\sum_{x=1}^{n} \left(f(x) - \hat{f}(x)\right)^2}{\sum_{x=1}^{n} \left(f(x) - \bar{f}(x)\right)^2},$$

  where $\bar{f}$ is the average value of the numerical data. Its range is $0 - 1$ (for our fit function), where 1 means the model explains the variance perfectly.

- **Relative MAE**: Average error relative to the magnitude of numerical data:

  $$\frac{\sum_{x=1}^{n} \left|f(x) - \hat{f}(x)\right|}{\sum_{x=1}^{n} |f(x)|},$$

  where the value 0 means is a perfect (average) fit.

- **Relative RMSE**: Standard deviation of prediction errors, normalized by the mean of

numerical data:

$$\frac{\sqrt{\frac{1}{n}\sum_{x=1}^{n}\left(f(x)-\hat{f}(x)\right)^2}}{\bar{f}}.$$

When its 0, the standard deviation is 0%.

Mathematica We now fit the data on $\Delta\omega$ for $\ell = 17$ and $m_2 = 4m_1$ to the function (4.3.9) using NonlinearModelFit from Mathematica [40], and extract the values a, b and c. The result is:

$$f(x) = 0.463603 - \frac{0.504702}{1 + 148.653x^2}. \tag{4.3.10}$$

As we see, $a + b < 0$, which contradicts with our assessment that this function can explain the whole non-datationary behavior. But still $a > b$, which needs to be true for the non-adiabatic results to make sense. We can see the fit for $\ell = 17$ and its relative residuals in Figure 4.16, which also point to the fact that the function (4.3.9) can only describe the non-adiabatic properties. Also, the values for the goodness assessment are presented in Table 4.3.1.

Function (4.3.9) fitted on $\Delta\omega$ data for $\ell = 17$

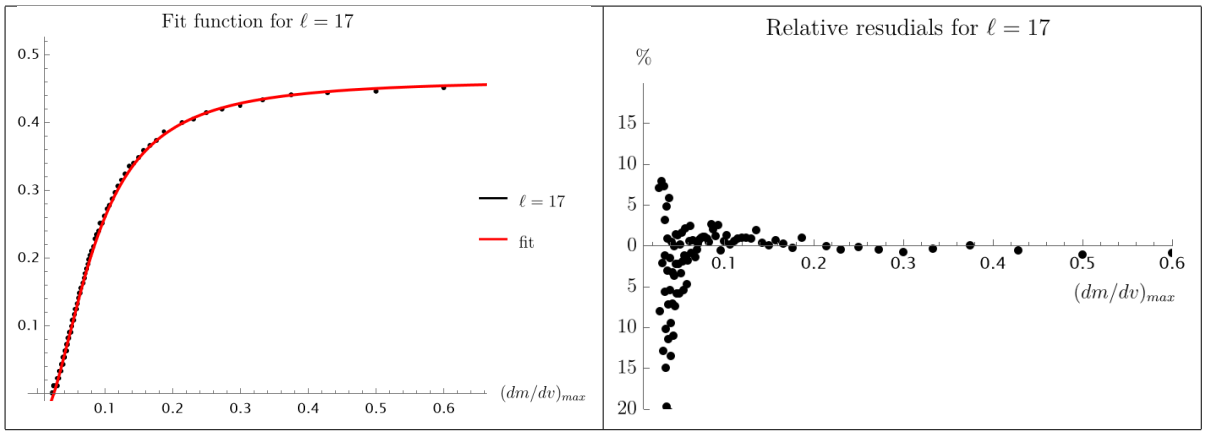

Figure 4.16: $\Delta\omega$ for $\ell = 17$ fitted against $(dm/dv)_{max}$ using the function (4.3.9). The fit (left) describes the data well in the non-adiabatic region, while the relative residuals (right) show that in breaks approaching the adiabatic region.

ℓ	R^2	Relative MAE	Relative RMSE
17	0.999238	0.0204931	0.025729

Table 4.3.1: Fit summary for $\ell = 17$, indicating a good fit.

Coefficient	Estimate	Standard Error	t-Statistic	P-Value
a	0.463603	0.00139079	333.339	4.76×10^{-158}
b	-0.504702	0.00138088	-365.494	3.65×10^{-162}
c	0.00672707	0.0000785171	85.6765	1.45×10^{-97}

Table 4.3.2: Fit parameters with standard errors, t-statistics, and P-values, indicating that all the parameters have importance in describing the functional dependence of $\Delta\omega$ on $(dm/dv)_{max}$.

Furthermore, we can see values connected to the parameters of the fit in table 4.3.2, showing the standard error, t-Statistic and P-Value. These values indicate that the parameters are

calculated with high precision and certainty that they are relevant. This analysis indicates the functional form (4.3.9) is well suited for analyzing the non-adiabatic behavior of a mass-changing black hole.

Once we have shown that the functional form (4.3.9) describes the non-adiabatic region with good precision, and we use it to examine the proposed scalings (4.3.7) and (4.3.8). For the fit, we again use results for $\ell = 17$ and $m_2 = 4m_1$, and focus only on the real part of QNFs.

First, we will focus on (4.3.8), fitting the rescaled $\ell = 17$ and $m_2 = 4m_1$ case, then rescaling all the others and calculating the aforementioned values to assess these fits. Doing the fit, we arrive to following function:

$$f(x) = 0.137039 - \frac{0.154287}{1 + 163.821x^2}. \tag{4.3.11}$$

One thing we can notice right away is that the biggest discrepancy from the static values of the QNMs is going to be $\approx 14\%$. But, this is only true for $m_2 = 4m_1$, and this value will be different for different m_2 due to the influence of $m(v)\omega(v) = \omega_0(\ell)$ on QNMs. The values assessing the goodness of the proposed dependence are represented in Table 4.3.3 and Figure 4.17. As can

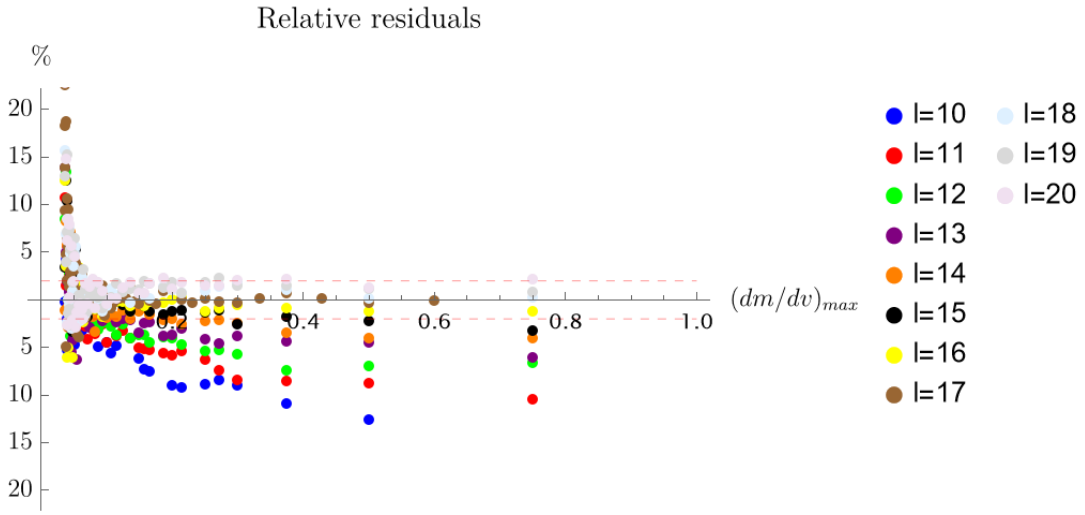

Figure 4.17: Relative residuals for the functional dependence proposed in (4.3.8), fitted to $\Delta\omega$ for $\ell = 17$, and assessed for all other $\Delta\omega$ rescaled by the proposed functional dependence. Red lines represent 2% deviation for the fit function. $\Delta\omega$ for $\ell > 15$ fit well, while the lower values deviate more, as expected.

be concluded from these values, the fit is quite good for high $\ell > 15$, but it worsens for low ℓ, as expected. On the other hand, the Relative residuals in Figure 4.17 show a regular behavior of the discrepancy, indicating that there is a missing functional dependence that can still be caught with further analysis, which is indeed proposed in (4.3.7).

We now fit using the full dependence on ℓ proposed in (4.3.7), for the same value of $\ell = 17$ and $m_2 = 4m_1$, and do the same analysis. This yields us the values in Table 4.3.4 and Figure 4.18.

These values show that indeed, this functional dependence is better for low ℓ's, but there is still a bit of regularity in the Relative residuals, showing that there can still be refinements to this analysis. Also, we see that the fit breaks down for low $(dm/dv)_{max}$, indicating that truly

ℓ	R^2	Relative MAE	Relative RMSE
10	0.977	6.244	9.647
11	0.985	4.991	7.291
12	0.991	4.004	5.623
13	0.995	3.216	4.275
14	0.998	2.072	2.896
15	0.999	1.600	2.103
16	0.999	1.060	1.315
17	0.999	1.126	1.557
18	0.999	1.246	1.503
19	0.999	1.543	1.923
20	0.999	1.758	2.187

Table 4.3.3: Fit summary for (4.3.8). Data on $\ell = 17$ was fitted, and then assessed for $\ell = 10-20$. These values confirm that data on $\ell > 15$ fits well, and that we have a gradual worsening when lowering ℓ.

Fit function and $\Delta\omega$ for $\ell = 10 - 20$ scaled as proposed in (4.3.7)

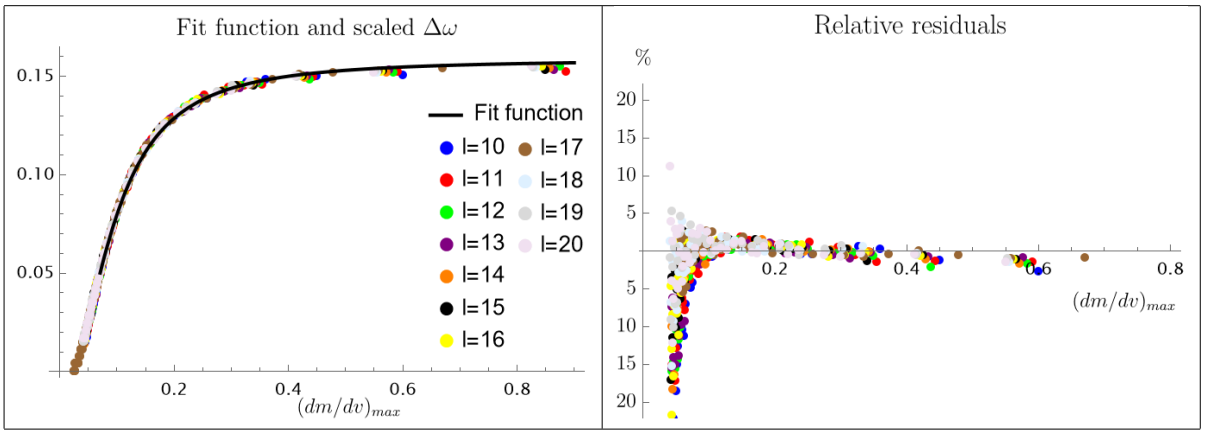

Figure 4.18: Function (4.3.9) fitted on $\Delta\omega$ for $\ell = 17$ and plotted against $\Delta\omega$ for $\ell = 10 - 20$ based on the functional dependence proposed in (4.3.12) (left), and the corresponding relative residuals (right). We see a better match to this proposed functional dependence than in (4.3.8).

(4.3.9) can describe only the non-adiabatic behavior.

4.3.5 Combining the results for all parameters of the background

Once we have analyzed the impact on different ℓ modes and found the function $f((dm/dv)_{max})$ that governs this behavior, we can comment on the proposed behavior of the non-adiabatic effect in QNFs induced by the mass change. Putting all the dependencies together we get:

$$m_1 \Delta\omega \propto \omega_0(\ell) \frac{l - 1.75}{l + 0.5} \left(\frac{8}{9}\right)^{\frac{m_2}{m_1}} f\left(\frac{l+2}{l} c_m (dm/dv)_{max}\right), \tag{4.3.12}$$

where:

$$(dm/dv)_{max} \propto \frac{m_2 - m_1}{[\sim \text{time of change}]}, \quad f(x) = 0.254109 - \frac{0.276636}{1 + 119.005x^2}. \tag{4.3.13}$$

Values for 4.3.12	R^2	**Relative MAE**	**Relative RMSE**
10	0.997043	0.0273218	0.0346572
11	0.998193	0.0221485	0.0251814
12	0.998669	0.0175136	0.0218076
13	0.998696	0.0171743	0.0217866
14	0.999052	0.0148010	0.0186704
15	0.999141	0.0146899	0.0177862
16	0.999172	0.0145548	0.0176879
17	0.999321	0.00888417	0.0108215
18	0.999427	0.0119560	0.0147284
19	0.999485	0.0115842	0.0139803
20	0.999484	0.0114940	0.0140280

Table 4.3.4: Fit summary for (4.3.7). Data on $\ell = 17$ was fitted, and then assessed for $\ell = 10-20$. This values point to the fact that the proposed dependence goes in the right direction in unifying this phenomena.

We see that maximum value of the discrepancy for (4.3.12) turns out to be $\approx 25\%$ (from the initial value of the QNFs). The parameters appearing in the expression (4.3.12) are as follows: $\omega_0(\ell)$ is the value of the QNMs for different ℓ's, c_m is the scaling required for generalization to different mass profiles, m_2 is the final mass, m_1 is the initial mass, and [$\sim$ time of change] holds the information about the duration of accretion. We can conclude a few things from these rescalings:

- $\omega_0(\ell)$ - non-adiabatic effect grows with the increase of the value of QNFs $\rightarrow$ higher frequency modes are fractionally more influenced, and are the ones that will have more inertia
- m_1 - scale of the system - we showed that (4.3.12) obeys the scale of the system, as m_1 is present in proper places
- m_2 - has two influences:
  - it influences the dynamical behavior of the background. If this higher, it increases the non-adiabatic effects
  - since the stationary expression $m(v)\omega(v) = \omega_0(\ell)$ guides the modes through the mass change, we have an additional contribution that lowers $\Delta\omega$ (by the same process occurring for $\omega_0(\ell)$)
- [$\sim$ time of change] - if the duration of accretion is shorter (for the same final mass), we get a more dynamical spacetime, and in turn an increase of non-adiabatic effects
- ℓ - we see that the dependence on ℓ has the same eikonal properties as the modes themselves, showing that there is no "new" behavior
- c_m - a constant that captures how to generalize the behavior for different mass profiles. No general prescription was found to calculate it, but was shown that this behavior is unified for different mass profiles.

- $f((dm/dv)_{max})$ - we see that we have a maximum value of $\Delta\omega_{scaled} \approx 25\%$, which shows that $\Delta\omega$ wont tend to infinity for extremely dynamical spacetimes

This analysis shows that there exists a unified description of the non-adiabatic effects in QNMs induced by a mass change of a black hole. Next to this, we are still missing a consistent choice of normalization for $(dm/dv)_{max}$, and a more precise values of the constants appearing in (4.3.12), whose improvement is discussed in the next section. Nonetheless, this can be regarded as a first attempt at describing the connection between non-adiabatic effects in QNMs induced by a mass change of a black hole, and serves as a guide for any future numerical and analytical studies.

5 Discussion

Through this thesis, we explored non-adiabatic effects in the relaxation of a mass-changing black hole. To set the stage and introduce the main concepts regarding the theory, we started by the analysis of gravitational waves and black holes. We showed how they arise from the theory, highlighted their main properties and explained their importance for this work. Once we had a good grasp on these objects, we turned to black hole perturbation theory. Here, we derived covariant and gauge invariant equations that hold information about first-order perturbations of a spherically-symmetric spacetime with arbitrary matter content. These covariant equations govern the dynamics we are interested in, and provided a backbone for the exploration of spacetimes considered in this project. To obtain a reference point for the phenomena induced by the changing mass, we focused on extensively studied perturbations of a static spherically-symmetric black hole. We showed general properties of its perturbation equations and introduced boundary conditions that gave us solutions that are identified as quasinormal modes. We calculated the corresponding values of quasinormal mode frequencies ω using a technique developed by Leaver [3]. A well known result, based on dimensional arguments and scale invariance, is that the QNFs are connected to the mass of the black hole as $m\omega = \omega_0(n, \ell)$ where $\omega_0(n, \ell)$ is a dimensionless value representing how the QNFs depend on the overtone number n and the multipolar index ℓ. This relation served as a reference in exploring the effects induced by a mass change. Having a good grasp on the solutions of the perturbation equations for a static black hole, we turned to the analysis of the QNFs of a mass-changing black hole.

5.1 Summary of results on the relaxation of Vaidya spacetime

The main results of this thesis come from exploring quasinormal modes of a Vaidya black hole. We used a numerical algorithm to solve the background equations of this spacetime along with the corresponding first-order perturbation equation, and obtained a solution for the master variable $\Psi(u, v)$ on a $u \times v$ grid. After we obtained these solutions, we explored how the mass change influences the properties of the background and the effective potential, which provided a description that encapsulates the similarities to the static case and highlighted the differences. Having an intuition of the Vaidya spacetime, we turned to the solution for $\Psi(u, v)$, extracting it at the horizon $\Psi_{\mathcal{H}} \equiv \Psi(u_{max}, v)$ and obtaining QNFs from it using the (4.2.6) algorithm. The modes at the horizon showed that the static expression $m(v)\omega(v) = \omega_0(\ell)$ guides them in their evolution, but there is an additional inertial behavior in the transient region, with a

minimum extending below the final value of the QNF. We used this minimum to construct a variable $\Delta\omega = \omega_{final} - \omega_{min}$ that holds information about the non-adiabatic effects present in the modes. The analysis showed that these values are different for the real and imaginary parts of the modes by $\Delta\omega_I/\omega_{0I} \approx 2\Delta\omega_R/\omega_{0R}$, but that they have the same dependence on the dynamics of the background. Once we had a measure of these non-adiabatic effects, we extracted QNFs and calculated $\Delta\omega$ for many different accretion scenarios, where the magnitude of their dynamics was measured with $(dm/dv)_{max}$. This analysis included changing the initial mass m_1, final mass m_2, duration of accretion [$\sim$ time of change], different mass profiles (governed by the constant c_m), and the most extensively studied multipolar index ℓ which was showed to be connected to its QNFs $\omega_0(\ell)$. This analysis led us to the following dependence of $\Delta\omega$ on these parameters:

$$m_1\Delta\omega \approx \omega_0(\ell)\frac{l-1.75}{l+0.5}\left(\frac{8}{9}\right)^{\frac{m_2}{m_1}} f\Big(\frac{l+2}{l}c_m(dm/dv)_{max}\Big), \tag{5.1.1}$$

where:

$$(dm/dv)_{max} \propto \frac{m_2-m_1}{[\sim \text{ time of change}]}, \quad f(x) = 0.254109 - \frac{0.276636}{1+119.005x^2}. \tag{5.1.2}$$

This equation is valid for for $\ell > 8$ and holds information on the behavior of the non-adiabatic effects induced by a mass change. The parameters appearing in the expression are as follows: $\omega_0(\ell)$ is a parameter representing the value of the QNMs for different ℓ's, c_m is the scaling required to generalize to different mass profiles and m_2 is the final mass, m_1 sets the scale of the system and [$\sim$ time of change] holds the information about the duration of accretion. In the eikonal limit, equation (5.1.1) (and fixing the mass profile so $c_m = 1$) we arrive to the following dependence:

$$m_1\Delta\omega \approx \omega_0(\ell)\left(\frac{8}{9}\right)^{\frac{m_2}{m_1}} f\Big((dm/dv)_{max}\Big), +. \tag{5.1.3}$$

This equation looks more tidy and removes some of the constants that we imposed in the model. The constrain is that (5.1.3) can explain the dependence for $\ell > 15$.

Equations (5.1.1) and (5.1.3) describe the behavior of non-adiabatic effects induced by a mass change of a black hole. They show that the non-adiabatic effect grows as the spacetime becomes more dynamical, and that there is a general behavior in the large ℓ limit. We also see that the maximum discrepancy from the initial values of QNFs is $\approx 25\%$. Additionally, they point to the fact that the connection between these to phenomena can be generalized to many spacetimes, needing only one function to describe a plethora of dynamical processes. This dependence can be regarded as a first attempt of describing this behavior and connecting the two phenomena in a systematic way.

The value that needs more study is the measure of how dynamical the spacetime is $(dm/dv)_{max}$, which holds information on the timescale of the background change. The question is how to properly normalize it, or in other words, to what phenomena from QNMs do we compare it to? The meaningful comparison we found is to compare it to the imaginary part of QNMs ω_{0I} (also constructed dimensionless), which controls the lifetime of the modes. This comparison gives us the interpretation is follows: if $(dm/dv)_{max}/\omega_{0I} \approx 1$ the two timescales are similar in value and we have a high influence on the non-adiabatic properties, meaning that any deviation for this

value would lead to big changes in $\Delta\omega$. If $(dm/dv)_{max}/\omega_{0I} \ll 1$, we are in the adiabatic regime, and if $(dm/dv)_{max}/\omega_{0I} \gg 1$, spacetime is so dynamical that modes cannot follow, giving rise to non-adiabatic effects.

5.2 Possible improvements and future analysis

In the end, we can discuss possible improvements to the analysis presented and the direction going forward.

From the numerical point of view, there are two things that can be improved. The more straightforward one is increasing the grid resolution Δ_u and Δ_v. This would give us a more precise solution for Ψ, and more importantly, improve the precision of the extraction algorithm (4.2.6). Since we have shown a general behavior in the eikonal (high frequency) limit, this would provide an opportunity to precisely test the current results, and extend the analysis to modes higher than $\ell = 20$. A more involved one is improving the algorithm we use to extract the frequencies and decay rates (4.2.6). This algorithm only allows us to capture these values from the maximums, minimums and zero crossing of Ψ. This poses a few problems regarding different phenomena. Firstly, for highly dynamical spacetimes, where the accretion of matter happens faster than one oscillation period, there is no way of capturing any processes in the transient region. We were able to probe this by extrapolation, but the direct measurement of this regime is hidden from this kind of algorithm. Secondly, there is no consistent way of placing the extracted frequencies such that they match perfectly in time with the mass change, which makes measuring the non-adiabatic behavior based on the minimum of the extracted frequency the only consistent choice when using this algorithm. Lastly, we would like to sample the modes in this region with as small time-steps as possible, translating to high frequency. But, as we discussed, higher frequencies are more prone to numerical errors. All these problems come from an algorithm based only on the the maximums, minimums and zero crossing, and to get around them one should try to approach this extraction in different way.

Finally, we comment on the improvements of the proposed dependence of non-adiabatic effects on the parameters of the background. This dependencies were found based on the analysis described in Appendix D. We only found the functional form which these dependencies should follow, but all the constants present were not rigorously calculated. There is an explanation in the Appendix D on how this could be done, but it was not implemented in this work. Also, there is a real chance for some of these dependencies to be captured by an analytic model of this phenomena. Since we see a unified dependence in the eikonal limit, it might be possible to capture these non-adiabatic effects in a large ℓ expansion. This limit is expected to simplify the equations, and since the lifetime of the modes remains constant (dictated by the damping rate) in this limit (3.3.23), we would have an explicit quantity to compare with the timescale of the background.

A Spherical harmonics

In this appendix we will introduce the scalar, vector, and tenor spherical harmonic that are used in the decomposition of the metric tensor [13]. These harmonics refer to a unit 2-sphere and the metric Ω_{AB} and its inverse Ω_{AB} are used to lower and raise indices. Any covariant differentiations in this appendix will refer to this metric.

We start with the well known scalar harmonics and the usual spherical-harmonic functions Y^{lm} which satisfies the following eigenvalue equation:

$$\big(\Omega^{AB} D_A D_B + \ell(\ell+1)\big) Y^{\ell m} = 0. \tag{A.0.1}$$

Using the scalar harmonics and its governing function Y^{lm} we can construct vector and tenor harmonics. They will come in two types, regarding their symmetry properties under parity. This in turn gives us two sectors of our perturbation equations, as discussed in the main text.

Vectorial spherical harmonics have an even-parity and an odd-parity harmonics:

$$Y^{\ell m}_A := D_A\, Y^{\ell m}, \tag{A.0.2}$$
$$X^{\ell m}_A := -\,\varepsilon_A{}^B\, D_B\, Y^{\ell m}, \tag{A.0.3}$$

and their orthogonality relations take the form:

$$\int \bar{Y}^{\ell m}_A\, Y^{\ell' m'}_A\, d\Omega = \ell(\ell+1)\, \delta_{\ell\ell'}\delta_{mm'}, \tag{A.0.4}$$
$$\int \bar{X}^{\ell m}_A\, X^{\ell' m'}_A\, d\Omega = \ell(\ell+1)\, \delta_{\ell\ell'}\delta_{mm'}, \tag{A.0.5}$$
$$\int \bar{Y}^{\ell m}_A\, X^{\ell' m'}_A\, d\Omega = 0, \tag{A.0.6}$$

where an overbear indicates complex conjugation and $d\Omega$ is the usual element of the solid angle. We can notice that even- and odd-parity harmonics are always orthogonal.

Tensor harmonics also come in two parites, but now we have two sets of even-parity harmonics and one set of odd-parity harmonics:

$$U^{\ell}_{AB} := \Omega_{AB} Y_{\ell m}, \tag{A.0.7}$$
$$Y^{\ell m}_{AB} := \Big(D_A D_B + \tfrac{1}{2}\,\ell(\ell+1)\,\Omega_{AB}\Big)\, Y^{\ell m}, \tag{A.0.8}$$
$$X^{\ell m}_{AB} := -\tfrac{1}{2}\big(\varepsilon_A{}^C D_C D_B + \varepsilon_B{}^C D_C D_A\big)\, Y^{\ell m}. \tag{A.0.9}$$

They obey the following orthogonality relations:

$$\int \bar{Y}^{\ell m}_{AB}\, Y^{\ell' m'}_{AB}\, d\Omega = \tfrac{1}{2}(\ell-1)\ell(\ell+1)(\ell+2)\, \delta_{\ell\ell'}\delta_{mm'}, \tag{A.0.10}$$
$$\int \bar{X}^{\ell m}_{AB}\, X^{\ell' m'}_{AB}\, d\Omega = \tfrac{1}{2}(\ell-1)\ell(\ell+1)(\ell+2)\, \delta_{\ell\ell'}\delta_{mm'}, \tag{A.0.11}$$
$$\int \bar{Y}^{\ell m}_{AB}\, X^{\ell' m'}_{AB}\, d\Omega = 0, \tag{A.0.12}$$
$$\Omega^{AB} Y^{\ell m}_{AB} = 0 \;=\; \Omega^{AB} X^{\ell m}_{AB}. \tag{A.0.13}$$

where we notice the trend of odd- and even- sectors always being orthogonal. This fact makes the perturbation equations coming from these two sectors to decouple and allows us to investigate them separately. In addition to this fact, odd- and even- sector perturbation equations are isospectral [13], further justifying the study of only one sector.

B Derivation of equations governing Vaidya spacetime in double-null coordinates

In this appendix, we go trough the derivation of equation governing the Vaidya spacetime in double-null coordinates from Einstein filed equations, following [42]. The Vaidya spacetime is defined as:

$$G_{\mu\nu} = \Phi K_\mu K_\nu, \;\; K^\mu K_\mu = 0, \tag{B.0.1}$$

and double-null coordinates as:

$$ds^2 = -2f(u,v)dudv + r^2(u,v)d\Omega^2. \tag{B.0.2}$$

Substituting this line element into Einstein filed equations (B.0.1) leads us to the following components of the Einstein tensor:

$$G_{uv} = \frac{f + 2\partial_u r \partial_v r + 2r\partial^2_{uv} r}{r^2} = 0, \tag{B.0.3}$$

$$G_{uu} = 2(\partial_u f \partial_u r/f - \partial^2_{uu} r)/r = 0, \tag{B.0.4}$$

$$G_{vv} = 2(\partial_v f \partial_v r/f - \partial^2_{vv} r)/r = \Phi. \tag{B.0.5}$$

From G_{uu} component:

$$\frac{\partial_u f}{f} = \frac{\partial_u \partial_u r}{\partial_u r}, \tag{B.0.6}$$

which, after integration over u gives:

$$f(u,v) = 2B(v)\partial_u r, \tag{B.0.7}$$

where $B(v)$ is a free function coming from integration over u. Next, we differentiate (B.0.3) with respect to u and substitute the equation (B.0.4) to get:

$$\partial_u \left(\frac{r^2 \partial^2_{uv} r}{f} \right) = 0 \rightarrow \frac{r^2 \partial^2_{uv} r}{f} + A(v) = 0, \tag{B.0.8}$$

where $A(v)$ again comes from integration over u. Differentiating (B.0.3) with respect to v and substituting (B.0.4), (B.0.5) and (B.0.8) gives:

$$\partial_v r = -B(v)\left(1 - \frac{2A(v)}{r}\right), \quad B(v) = \frac{f(u,v)}{2\partial_u r}. \tag{B.0.9}$$

Differentiating (B.0.3) w.r.t. v and substituting (B.0.5) and (B.0.8) gives:

$$\Phi = 2\frac{\partial_v A \partial_{uv}^2 r}{A \partial_u r}. \tag{B.0.10}$$

Next, substituting (13) and (14) into (15) gives:

$$\Phi = -4B(v)\frac{\partial_v A}{r^2}. \tag{B.0.11}$$

Defining:

$$B(v) = -2\frac{A(v)}{|A(v)|}, \tag{B.0.12}$$

allows the interpretation of $A(v)$ as mass profile $m(v)$. Another way to get the mass function is to observe that the Einstien equations allow a free function of v, which we can define in the following way:

$$m(v) = \frac{1}{2}r^3 R^{\theta\phi}{}_{\theta\phi} = \frac{r}{2f}(f + 2\partial_u r \partial_v r) \tag{B.0.13}$$

Differentiating this with respect to u shows that it does not depend on u, as desired. Defining $B(v) = \varepsilon$ and $A(v) = m(v)$, we arrive to the equations presented in the main text.

C Deriving the odd sector perturbation equation for Vaidya spacetime

In this appendix we will go through the derivation of the perturbation equation for Vaidya spacetime from the covariant odd sector perturbation equations and show how the Master variable Ψ relates to gravitational wave polarizations h [25]. Covariant odd sector perturbation equations have the form:

$$r^2 \nabla_a \left(r^{-2}\nabla^a (r\Psi)\right) - \frac{\lambda^2 - 2}{r}\Psi = r^2 \epsilon^{ab} K_b \nabla_a (\Phi\tilde{v}), \tag{C.0.1}$$

$$K^a \nabla_a \left(r^2 \Phi \tilde{v}\right) = 0, \quad \nabla_a j^a = 0. \tag{C.0.2}$$

These equations live on $\mathcal{N}^2$ which is governed by the metric g_{ab} with the components $g_{01} = g_{10} = -f(u,v)$ and $g_{00} = g_{11} = 0$. We will be able to use the background equations:

$$\partial_v r = -\varepsilon\left(1 - \frac{2m(v)}{r}\right), \quad \partial_u r = 2\varepsilon f(u,v), \quad \partial_{uv}^2 r = -\frac{m(v)f(u,v)}{r^2}, \tag{C.0.3}$$

to substitute any derivatives over $r(u,v)$ with algebraic expressions, simplifying the final perturbation equation considerably, where the value of ε is $\pm 1/2$. We can evaluate any contracted indices as follows: $K^a \nabla_a = g^{ab} K_b \nabla_a = -f^{-1}\partial_u$, where $g^{01} = g^{10} = -f^{-1}$, $g^0 = g^{11} = 0$ and $K_a = (0,1)$, or use any available software for this.

We start the derivation with the first equation in (C.0.2) with the goal of solving for $\tilde{v}$. We

can use the solution for $K^a\nabla_a$ from the above example and get:

$$\frac{\partial}{\partial u}\Big(r^2\Phi\tilde{v}\Big) = 0. \tag{C.0.4}$$

Integrating both sides over u we obtain:

$$\tilde{v} = \frac{F(v)}{r^2\Phi}, \tag{C.0.5}$$

where $F(v)$ is a integration function, connected to first order matter perturbation induced by null dust. This gives us the exact solution for $\tilde{v}$ and is as far as we need to go concerning equations in (C.0.2). We can now move to the equation (C.0.1), where we will first focus on simplifying the first term, which yields:

$$\begin{aligned} r^2\nabla_a\left(r^{-2}\nabla^a\left(r\Psi\right)\right) &= r^2\nabla_a\left[r^{-2}\left(\nabla^a r\Psi + r\nabla^a\Psi\right)\right] \\ &= r^2\nabla_a\left(r^{-2}\nabla^a r\right)\Psi + \nabla_a r\nabla^a\Psi \\ &+ r^2\nabla_a(r^{-1})\nabla^a\Psi + r\nabla_a\nabla^a\Psi. \end{aligned} \tag{C.0.6}$$

Two middle terms cancel and the last one evaluates to:

$$r\nabla_a\nabla^a\Psi = -\frac{2r}{f(u,v)}\partial^2_{uv}\Psi. \tag{C.0.7}$$

We are left with evaluating the first term, where we use (C.0.3) to reduce any derivatives over $r(u,v)$:

$$r^2\nabla_a\left(r^{-2}\nabla^a r\right) = -2r^{-1}\nabla_a r\nabla^a r + \nabla_a\nabla^a r \tag{C.0.8}$$

$$= 4r^{-1}\frac{\partial_v r\partial_u r}{f} - \frac{2\partial_u\partial_v r}{f} \tag{C.0.9}$$

$$= \frac{-8\varepsilon^2}{r}\Big(1 - \frac{2m(v)}{r}\Big) + 2\frac{m(v)}{r^2} \tag{C.0.10}$$

$$= -\frac{2}{r} + \frac{6m}{r^2}, \tag{C.0.11}$$

where we used ε^2=1/4. With all this, left side of (C.0.1) evaluates to:

$$\frac{-2r}{f}\left(\partial^2_{uv} - \frac{f}{r}\left(\frac{3m(v)}{r^2} - \frac{(\ell(\ell+1)}{2r}\right)\right)\Psi(u,v). \tag{C.0.12}$$

The last thing we need to do is evaluate the right side of (C.0.1):

$$r^2\varepsilon^{ab}K_b\nabla_a\left(\Phi\tilde{v}\right) = \frac{-r^2}{f}\partial_u\left(\frac{F(v)}{r^2}\right) = \frac{2}{rf}\partial_u rF(v) = \frac{4\varepsilon}{r}F(v), \tag{C.0.13}$$

where $\varepsilon^{uv} = 1/f$ and $K_u = 0$. Finally, we can connect (C.0.12) and (C.0.13) to obtain the odd sector perturbation equation for Vaidya spacetime:

$$\left(\partial^2_{uv} - \frac{f}{r}\left(\frac{3m(v)}{r^2} - \frac{(\ell(\ell+1)}{2r}\right)\right)\Psi(u,v) = \frac{2f}{r^2}\varepsilon F(v). \tag{C.0.14}$$

This equation coincides exactly with the result reported in [25] and governs the dynamics of the central problem examined in this thesis.

We can conclude this analysis by relating Ψ to the gravitational wave polarizations of the axial sector, h_+ and $h_\times$. The leading term of the axial metric fluctuation close to infinity in the radiation gauge for an ingoing radiation field, by the same arguments of [13] is:

$$h^{\rm rad} = r \sum_\ell \Psi^\ell_{\rm rad}(u)\, W^\ell{}_{AB}\, dz^A dz^B\,, \tag{C.0.15}$$

where:

$$\Psi^\ell_{\rm rad}(u) \equiv -\frac{4}{(\ell-1)(\ell+2)}\,\Psi^\ell(u, r=\infty)\,, \tag{C.0.16}$$

where we need to additionally assume that the in–falling wave does not extend to future null infinity, as is the case for us. This allows us to extract h_+ and $h_\times$ yeilding:

$$\begin{aligned} h_+ &\equiv \frac{h^{\rm rad}_{\theta\theta}}{r^2} = \frac{1}{r}\sum_\ell \Psi^\ell_{\rm rad}(u)\, W^\ell{}_{\theta\theta}\,, \\ h_\times &\equiv \frac{h^{\rm rad}_{\theta\phi}}{r^2\sin\theta} = \frac{1}{r\,\sin\theta}\sum_\ell \Psi^\ell_{\rm rad}(u)\, W^\ell{}_{\theta\phi}\,. \end{aligned} \tag{C.0.17}$$

D Method of gaining the functional dependence on different parameters

We will go through the method for gaining insight of the functional dependence on different parameters of the problem. We will use the ℓ parameter to enforce the ideas since it will provide a simple linear dependence, suitable for this example. As we can see from the main text, this dependence will be physically more involved, since we have contributions from $\omega_R \sim \ell\Omega$, but we will still focus in the linear nature connected to ℓ for simplicity. We start by fitting the function:

$$f(x) = a + \frac{b}{1 + x^2/c}, \tag{D.0.1}$$

to different curves representing behaviors for different ℓ's. We then extract the values of a, b and c. Plotting these values, we see that a and $-b$ grow linearly with increasing ℓ. This points to the dependence of the form:

$$\Delta\omega \approx l f(x). \tag{D.0.2}$$

A brute force way to obtain the dependence (what is used here) is to propose a dependence on this parameter based on the inspection of the plots, scale our data with it, and fit again. Repeat this until you get constant values of the fit across the parameter range, or at least within their error estimate. To get the exact expression, we can fit the behavior of the values, in this case the linear behavior, extract it's parameters and based on this rescale the initial data.

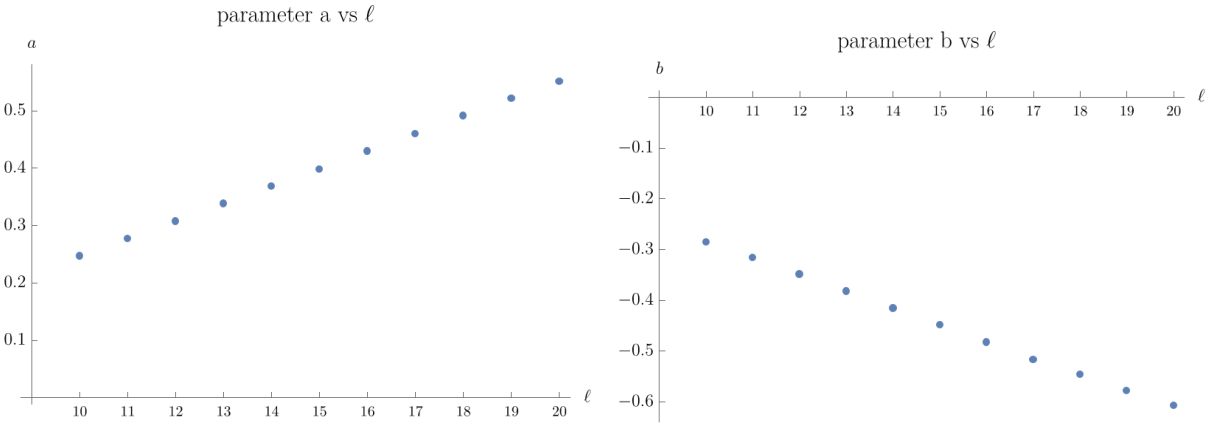

Figure D.1: Plots of the parameter a and b from the function (4.3.9), fitted on $\Delta\omega_R$ for $\ell = 10 - 20$ with the goal of extracting the dependence on ℓ.

References

[1] S.M. Carroll, *Spacetime and Geometry: An Introduction to General Relativity*, Addison-Wesley, San Francisco (2004).

[2] R. Ruffini and J.A. Wheeler, *Introducing the black hole*, *Physics Today* **24** (1971) 30 [https://pubs.aip.org/physicstoday/article-pdf/24/1/30/8273282/30_1_online.pdf].

[3] E.W. Leaver, *An Analytic representation for the quasi normal modes of Kerr black holes*, *Proc. Roy. Soc. Lond. A* **402** (1985) 285.

[4] E.W. Leaver, *Spectral decomposition of the perturbation response of the Schwarzschild geometry*, *Phys. Rev. D* **34** (1986) 384.

[5] T. Regge and J.A. Wheeler, *Stability of a schwarzschild singularity*, *Phys. Rev.* **108** (1957) 1063.

[6] F.J. Zerilli, *Effective potential for even-parity regge-wheeler gravitational perturbation equations*, *Phys. Rev. Lett.* **24** (1970) 737.

[7] B.L. Webster and P. Murdin, *Cygnus x-1: A spectroscopic binary with a heavy companion.*, *Nature (London) 235: No. 5332, 37-8(7 Jan 1972).* (1972) .

[8] LISA Consortium Waveform Working Group collaboration, *Waveform Modelling for the Laser Interferometer Space Antenna*, 2311.01300.

[9] T.W. Baumgarte and S.L. Shapiro, *Numerical Relativity: Solving Einstein's Equations on the Computer*, Cambridge University Press (2010).

[10] L. Blanchet, *PostNewtonian theory and its application*, in *12th Workshop on General Relativity and Gravitation*, 4, 2003 [gr-qc/0304014].

[11] E. Berti, V. Cardoso and A.O. Starinets, *Quasinormal modes of black holes and black branes*, *Class. Quant. Grav.* **26** (2009) 163001 [0905.2975].

[12] C. Palenzuela, *Introduction to Numerical Relativity*, *Front. Astron. Space Sci.* **7** (2020) 58 [2008.12931].

[13] K. Martel and E. Poisson, *Gravitational perturbations of the Schwarzschild spacetime: A Practical covariant and gauge-invariant formalism*, *Phys. Rev. D* **71** (2005) 104003 [gr-qc/0502028].

[14] D. Pereñiguez, *Black hole perturbations and electric-magnetic duality*, *Phys. Rev. D* **108** (2023) 084046 [2302.10942].

[15] E. Berti, V. Cardoso, J.A. Gonzalez, U. Sperhake, M. Hannam, S. Husa et al., *Inspiral, merger and ringdown of unequal mass black hole binaries: A Multipolar analysis*, *Phys. Rev. D* **76** (2007) 064034 [gr-qc/0703053].

[16] A. Buonanno, G.B. Cook and F. Pretorius, *Inspiral, merger and ring-down of equal-mass black-hole binaries*, *Phys. Rev. D* **75** (2007) 124018 [gr-qc/0610122].

[17] R. Cotesta, A. Buonanno, A. Bohé, A. Taracchini, I. Hinder and S. Ossokine, *Enriching the Symphony of Gravitational Waves from Binary Black Holes by Tuning Higher Harmonics*, *Phys. Rev. D* **98** (2018) 084028 [1803.10701].

[18] E. Berti, V. Cardoso and C.M. Will, *On gravitational-wave spectroscopy of massive black holes with the space interferometer LISA*, *Phys. Rev. D* **73** (2006) 064030 [gr-qc/0512160].

[19] H. Yang, D.A. Nichols, F. Zhang, A. Zimmerman, Z. Zhang and Y. Chen, *Quasinormal-mode spectrum of Kerr black holes and its geometric interpretation*, *Phys. Rev. D* **86** (2012) 104006 [1207.4253].

[20] A. Zhidenko, *Quasinormal modes of Schwarzschild de Sitter black holes*, *Class. Quant. Grav.* **21** (2004) 273 [gr-qc/0307012].

[21] R.A. Konoplya and A. Zhidenko, *Quasinormal modes of black holes: From astrophysics to string theory*, *Rev. Mod. Phys.* **83** (2011) 793 [1102.4014].

[22] V. Cardoso, K. Destounis, F. Duque, R.P. Macedo and A. Maselli, *Black holes in galaxies: Environmental impact on gravitational-wave generation and propagation*, *Phys. Rev. D* **105** (2022) L061501 [2109.00005].

[23] L. Sberna, P. Bosch, W.E. East, S.R. Green and L. Lehner, *Nonlinear effects in the black hole ringdown: Absorption-induced mode excitation*, *Phys. Rev. D* **105** (2022) 064046 [2112.11168].

[24] P. Vaidya, *The Gravitational Field of a Radiating Star*, *Proc. Natl. Inst. Sci. India A* **33** (1951) 264.

[25] J. Redondo-Yuste, D. Pereñiguez and V. Cardoso, *Ringdown of a dynamical spacetime*, *Phys. Rev. D* **109** (2024) 044048 [2312.04633].

[26] E. Abdalla, C.B.M.H. Chirenti and A. Saa, *Quasinormal modes for the Vaidya metric*, *Phys. Rev. D* **74** (2006) 084029 [gr-qc/0609036].

[27] I. Hawke, L. Baiotti, L. Rezzolla and E. Schnetter, *Gravitational waves from the 3d collapse of a neutron star to a kerr black hole*, *Computer Physics Communications* **169** (2005) 374.

[28] H.M. Siahaan and Triyanta, *Hawking Radiation from a Vaidya Black Hole: A Semi-Classical Approach and Beyond*, in *2nd International Conference on Mathematics and Natural Sciences (ICMNS)*, 11, 2008 [0811.1132].

[29] S.W. Hawking, *Black hole explosions*, *Nature* **248** (1974) 30.

[30] H. Reall, *General Relativity 2012 Harvey Reall Lecture Notes*, Scribd (2012).

[31] Wikipedia contributors, *Killing horizon — wikipedia, the free encyclopedia*, 2024.

[32] H. Stephani, D. Kramer, M. MacCallum, C. Hoenselaers and E. Herlt, *Solutions with groups of motions*, in *Exact Solutions of Einstein's Field Equations*, Cambridge Monographs on Mathematical Physics, Cambridge University Press (2003).

[33] P.M. Morse and H. Feshbach, *Methods of Theoretical Physics*, McGraw-Hill, New York (1953).

[34] E. Berti and V. Cardoso, *Quasinormal ringing of Kerr black holes. I. The Excitation factors*, *Phys. Rev. D* **74** (2006) 104020 [gr-qc/0605118].

[35] D. Philipp and V. Perlick, *On analytic solutions of wave equations in regular coordinate systems on Schwarzschild background*, 1503.08101.

[36] V. Ferrari and B. Mashhoon, *New approach to the quasinormal modes of a black hole*, *Phys. Rev. D* **30** (1984) 295.

[37] Event Horizon Telescope collaboration, *First M87 Event Horizon Telescope Results. I. The Shadow of the Supermassive Black Hole*, *Astrophys. J. Lett.* **875** (2019) L1 [1906.11238].

[38] W.A. Hiscock, *Models of evaporating black holes. i*, *Phys. Rev. D* **23** (1981) 2813.

[39] C. Gundlach, R.H. Price and J. Pullin, *Late time behavior of stellar collapse and explosions: 1. Linearized perturbations*, *Phys. Rev. D* **49** (1994) 883 [gr-qc/9307009].

[40] W.R. Inc., "Mathematica, Version 14.2."

[41] S. Horvát, *Matex*, Mar., 2024. 10.5281/zenodo.10828124.

[42] B. Waugh and K. Lake, *Double-null coordinates for the vaidya metric*, *Phys. Rev. D* **34** (1986) 2978.